LATVIAN JOURNAL of PHYSICS and TECHNICAL SCIENCES

ISSN 0868 - 8257

1

Institue of Physical Energetics-70

(Vol. 53)

2016

Ind. pasūt. € 1,50 Indekss 2091
Org. € 15,00 Indekss 2092

SATURS

ENERĢĒTIKAS FIZIKĀLĀS UN TEHNISKĀS PROBLĒMAS

CIETVIELU FIZIKA

LIETIŠĶĀ FIZIKA

Price to individual subscribers € 1.50/issue Index 2091
Price to collective subscribers € 15.00/issue Index 2092

CONTENTS

PHYSICAL AND TECHNICAL ENERGY PROBLEMS

SOLID STATE PHYSICS

APPLIED PHYSICS

Индивид. заказ. Є 1,50 Индекс 2091
Орг. заказ. Є 15,00 Индекс 2092

СОДЕРЖАНИЕ

ФИЗИКО-ТЕХНИЧЕСКИЕ ПРОБЛЕМЫ ЭНЕРГЕТИКИ

ФИЗИКА ТВЕРДОГО ТЕЛА

ПРИКДАДНАЯ ФИЗИКА

LATVIAN JOURNAL of PHYSICS and TECHNICAL SCIENCES

LATVIJAS FIZIKAS un TEHNISKO ZINĀTŅU ŽURNĀLS

ЛАТВИЙСКИЙ ФИЗИКО-ТЕХНИЧЕСКИЙ ЖУРНАЛ

Published six times a year since February 1964
Iznāk sešas reizes gadā kopš 1964. gada februāra
Выходит шесть раз в год с февраля 1964 года

1 (Vol. 53) • 2016

RĪGA

INDEKSĒTS (PUBLICĒTS) | INDEXED (PUBLISHED) IN

www.scopus.com
www.degruyter.com
EBSCO (Academic Search Complete, www.epnet.com), INSPEC (www.iee.org.com).
VINITI (www.viniti.ru), Begell House Inc/ (EDC, www.edata-center.com).

Izdevējs: Fizikālās enerģētikas institūts
Reģistrācijas apliecība Nr. 0221
Redakcija: Aizkraukles ielā 21, Rīga, LV-1006
Tel. 67551732, 67558694
e-pasts: ezerniec@edi.lv
Interneta adrese: www.fei-web.lv
Iespiests SIA “AstroPrint”

LATVIAN JOURNAL OF PHYSICS AND TECHNICAL SCIENCES
2016, N 1

DOI: 10.1515/lpts-2016-0001

PHYSICAL AND TECHNICAL ENERGY PROBLEMS

THE POTENTIAL OF RENEWABLE ENERGY SOURCES IN LATVIA

S. Sakipova[1, 2], A. Jakovics[2],
S. Gendelis[2]

[1]E.A.Buketov

Karaganda State University,
28 Universitetskaya Str., Karaganda, 100028, KAZAKHSTAN,
[2]Laboratory for Mathematical Modelling of Technological and
Environmental Processes, University of Latvia,
8 Zellu Str., Riga, LV-1002, LATVIA

The article discusses some aspects of the use of renewable energy sources in the climatic conditions prevailing in most of the territory of Latvia, with relatively low wind speeds and a small number of sunny days a year. The paper gives a brief description of the measurement equipment and technology to determine the parameters of the outer air; the results of the measurements are also analysed. On the basis of the data obtained during the last two years at the meteorological station at the Botanical Garden of the University of Latvia, the energy potential of solar radiation and wind was estimated. The values of the possible and the actual amount of produced energy were determined.

Keywords**:** *Betz-Zhukovsky criterion, intensity of solar radiation, potential, renewable energy resources, wind speed.*

1. INTRODUCTION

Currently, the technology for production of heat and electricity using renewable energy sources (RES) has become increasingly relevant. This owes to a continuous increase in the rate of energy consumption, rising prices for traditional energy sources, and environmental degradation. At present, the greatest interest is attracted to the technology using wind energy and solar radiation energy [1]–[4].

The modern level of technology using a variety of mono- and polycrystalline photo cells or polymer converters provides solar collectors of high efficiency [5]–[7]. There are examples of successful projects on the use of renewable energy sources in Latvia. For example, in the complex Sun Republic in the town of Saulkrasti solar collectors and photo batteries are installed, which minimise energy consumption for

water heating and contribute to the reduction of CO_2 emissions into the atmosphere [8]. Furthermore, the use of solar collectors affects favourably utility bills, which can reduce by 30 %. According to [9], the operational practice of Saulessukni EKTOS heating system, using vacuum solar collectors TS400, can save up to 85 % of the energy consumed for heating and hot water.

Owing to its geographical location and climate, the Baltic coast area is in a favourable condition to site wind farms in Latvia, as the wind speed here is relatively high. Many papers are published that consider the study of parameters of the wind in coastal areas, and analysis of physical and technical characteristics and economic performance of existing wind farms. In [10], the authors show the results of the study of seasonal variations of wind speed on the coast of the Baltic Sea in Latvia. Using approximating functions, the authors assess the energy potential of wind by processing statistical weather data of wind speed and density fluctuations at altitudes from 10 m to 160 m, obtained from long-term observations (2004–2013). In [11], the authors show that "power generation at offshore wind farms is by 25–40% greater than on land, in case they are placed at a distance of 3–5 km far from the coast where the weaker onshore wind transforms into a stronger sea wind, but not farther than 40 km." The profitability of surface wind farms also depends on the distance from the coastline, which is confirmed by the results of operation of two wind farms in Latvia: Uzhava (500 meters far from the sea) and Alsunga (13.5 km far from the sea) [12]. Wind turbines of 1 MW with a 60 m high tower are mounted at both farms. The analysis of parameters of wind and wind farm economic performance has shown that Uzhava WF, where the wind speed is greater by about 25 %, produces 2 times more electric power; its cost is 2 times lower than that in Alsunga.

Indeed, the wind power potential is strongly dependent on the speed, and as a rule, the wind speed of 3 m/s is not considered a possible energy source. However, the greatest part of the territory of Latvia as well as large cities with tall buildings are blown by a low-speed wind. In this article, the wind speed measurement data and that of intensity of solar radiation obtained in an urban environment of Riga are quoted. Their possible potential to use for the independent power supply of a small building or a house is estimated. The solution to this problem is challenging in many regions of Latvia where there are rural buildings or in small villages, the population of which, unfortunately, is decreasing and centralised electricity supply becomes unprofitable.

2. THE TECHNIQUE OF MEASURING THE PARAMETERS OF OUTER AIR AND SOLAR RADIATION LEVEL

Since April 2013 at the VTPMML Laboratory parameters of outer air in Riga have been monitored [13]. Gill instruments MetPak Pro weather station for measuring outer air parameters was erected at a height of 4.5 meters in the Botanical Garden of the University of Latvia. Compact multi-sensor weather station instrumentation makes it possible every moment to obtain basic parameters of the outer air: wind speed and its direction, temperature and relative humidity, atmospheric pressure, etc. on-line. The specifications and the accuracy of their measurements are given in Table 1.

Table 1

Specifications of MetPak Pro Weather Station Measurements

Denomination	Specifications	
Wind speed	Range:	0.01 to 60 m/s
	Accuracy:	± 2 % @ 12m/s
	Resolution:	0.01 m/s
	Threshold:	0.01 m/s
Wind direction	Range:	0 to 360º (no dead band)
	Accuracy:	± 3º @ 12 m/s
	Resolution:	1º
	Response time:	0.25 sec
Air temperature	Range:	-35ºC to +70ºC
	Accuracy:	± 0.1ºC
	Resolution:	0.1ºC

To determine the wind speed and its direction, the WindSonic ultrasound technology is used. The values of temperature, relative humidity and dew point are determined by the Rotronic HC2-S3 HygroClip sensor, which is protected from all forms of radiation by a case with a special coating. The sensor (piranometre) of the brand mark Hukseflux LP02 [15] measures the intensity of incident solar radiation and the associated thermal energy; characteristics are given in Table 2. The sensor measures the intensity of solar radiation, covering the entire visible range on a horizontal plane (the angle of 180°). This sensor can measure the intensity of the direct and reflected solar radiation, both indoors and outdoors.

Table 2

The Main Characteristics of the Solar Radiation Sensor

Parameter	Value
Response time for 95 % response	18 s
Sensitivity	10–40 μV/Wm^{-2}
Non-linearity	< +/- 2.5%
Directional response for beam radiation	within +/- 25 W/m^2
Spectral selectivity	+/- 5% (305 to 2000 nm)
Tilt response	within +/- 2%
Expected voltage output	0.1 to + 50 mV in natural sunlight
Sensor resistance	Between 40 and 60 Ohms

In addition to the outer air characteristics shown in the table, in [13], [14] detailed data on the measurement of other parameters such as atmospheric pressure, relative humidity of the air, etc. are given.

3. EXPERIMENTAL RESULTS

In general, during the year the climate in Latvia, and particularly, in Riga is characterised by variable clouds and high humidity. The amplitude of diurnal temperature changes is the interval from 10 °C to 17 °C; during the month the average

temperature varies within the range of (15÷22) °C (Fig. 1).

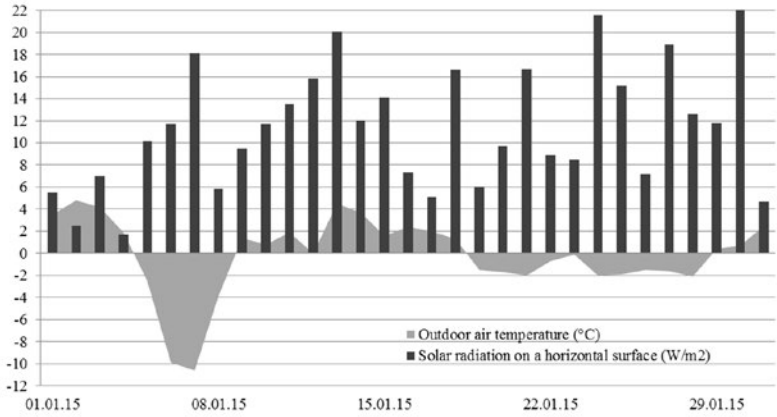

Fig. 1. Variation of the average outer temperature and intensity of solar radiation in January 2015 in Riga.

Mean monthly values of air temperature, wind speed and solar radiation intensity according to measurements in April 2013 are shown in Fig. 2. Analysis of the parameters of outer air in Riga shows that over the past two years, in Latvia the average yearly temperature has increased, and it is +8.04 °C. In the summer months the average air temperature is +17 °C, the average maximum is + 25.4 °C. The coldest months are January and February, when the average minimum temperature is -13.7 °C (Fig. 2a).

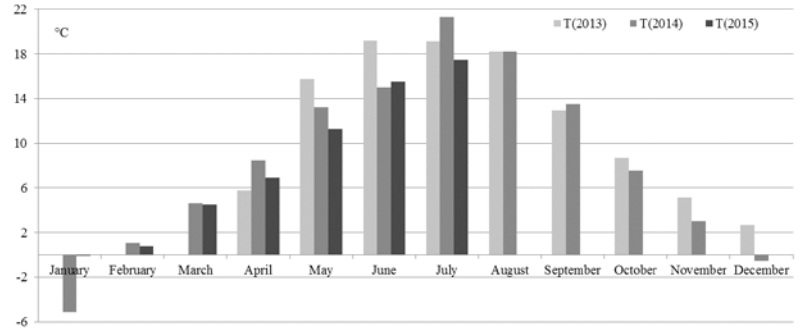

a)

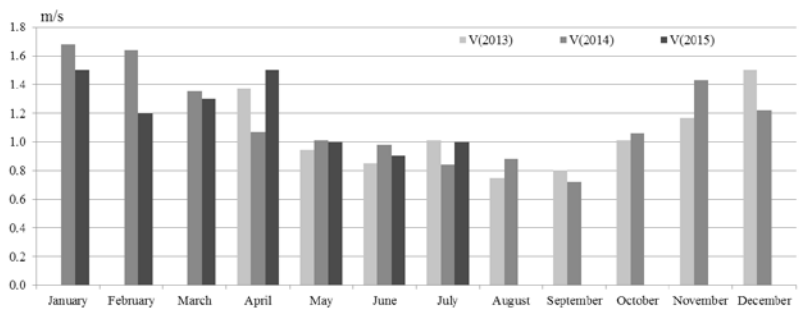

b)

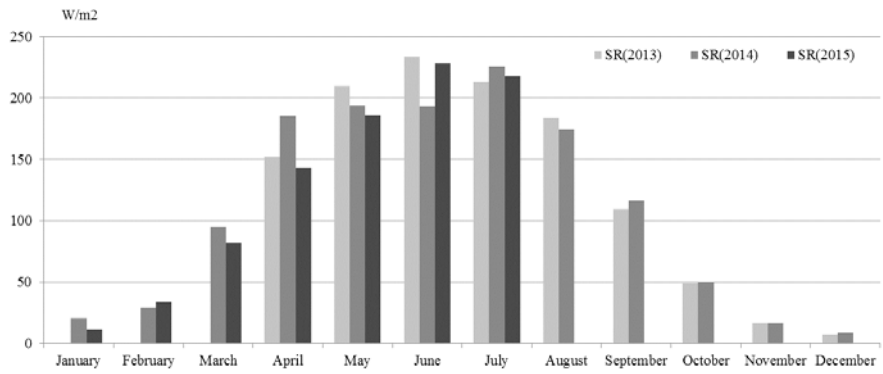

c)

Fig. 2. Average monthly values of the outer air parameters in Riga:
a) temperature; b) wind speed; c) intensity of solar radiation.

According to the results of the measurements, the average wind speed in Riga is 1.13 m/s (Fig. 2b). In the day-time and in the evening, the wind increases, low wind speed is observed mostly at night and in the early morning hours. The maximum speed of 5 m/s and greater is observed in the winter and autumn months, but this wind speed keeps not more than 2 % of the time.

As for intensity of solar radiation SR (Fig. 2c), its annual average level during 2 years is SR_{av} = 123 W/m^2. The reliability of the measurement results (Figs. 1, 2) is confirmed by the fact that in general they are consistent with on-line data of the operative information of the Latvian Centre for Environment, Geology and Meteorology [15]. Figure 3 shows the average monthly temperature of the outer air in Riga by different data.

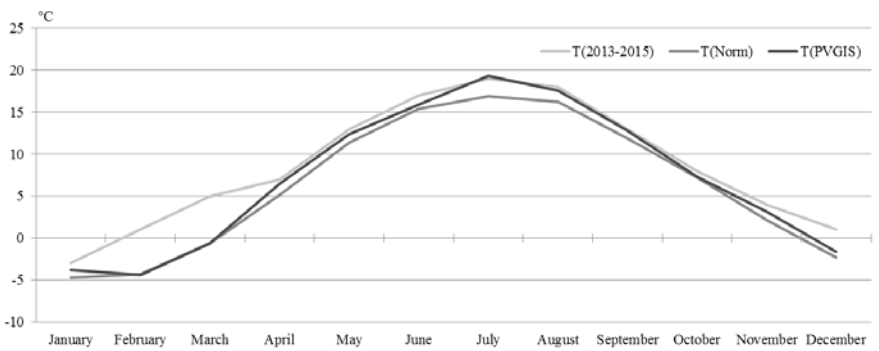

Fig. 3. Change of the average outdoor air temperature during the year in Riga.

Here T(2013–2015) represents our results of measurements [13], [14]; T(Norm) implies the data according to the site LBN 003-01 [16], which are used as regulatory standards in the calculations of the construction industry in Latvia; and T(PVGIS) is the data of the European Photovoltaic Geographical Information System [17], where the temperature values are calculated on the basis of the satellite system measurement data. It can be seen that in general the results of the outer

air temperature measurements are consistent with other data, the difference is only observed in the values of temperatures in February and March. This difference can be explained by the fact that the measured values of T(2013–2015) are obtained by averaging the measurements of the outer air temperature just in the last 2 years, while the values of T(Norm) and T(PVGIS) are determined on the basis of long-term observations of more than 10 years. In addition, it is well known that in recent years the climate warming in the winter has been observed not only in Latvia, but also in some European countries [1]–[3], [7].

4. EVALUATING POSSIBLE USE OF POTENTIAL OF RENEWABLE ENERGY SOURCES

The dynamic development of renewable power generation using renewable energy sources (RES) is due to the continuous increase in the cost of energy production. The maximum increase is observed in the decentralised power supply system specific to certain areas in Latvia, far from the central power supply lines, and autonomous energy systems running on imported fuel. The advantage of using renewable energy sources is determined by the efficiency of technology compared to traditional hydrocarbon sources; and cost-effective implementation of renewable energy depends essentially on the environmental conditions. Thus, an important role is played by the determination of the energy potential of a particular type of renewable energy in a particular locality.

4.1 Evaluation of the Solar Radiation Resource

To determine the amount of incident solar energy per 1 m^2 of horizontal surface in Riga during the day, we use the averaged results of measurements of the intensity of solar radiation. As can be seen from the diagram (Fig. 4), according to the changes in it, the results of the calculation of daily solar radiation W(2013–2015) are consistent with the data of PVGIS [17], but the values are slightly smaller (Fig. 4). Probably, this difference is due to the fact that the measurements of the intensity of solar radiation in the Botanical Garden were made at 4.5 m height, and the data [17] were calculated on the basis of the measurements obtained from the satellite.

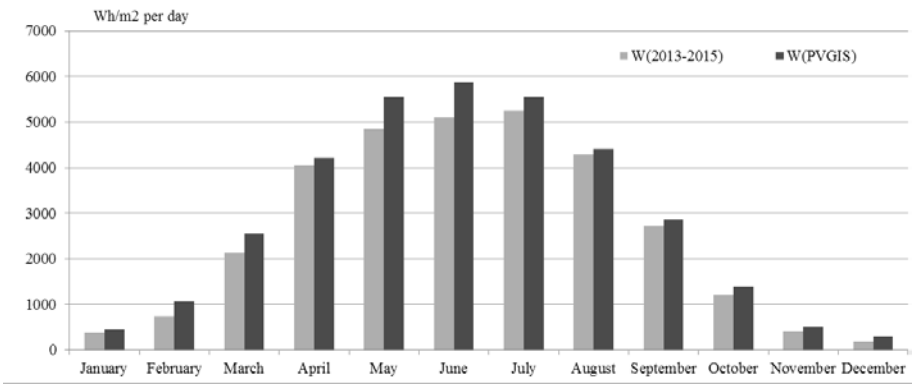

Fig. 4. Amount of energy of solar radiation per 1 m^2 of horizontal surface during the year.

Thus, due to the conversion of solar radiation in Riga it is possible to produce on average 954 κWh of energy per square meter a year. The resulted energy value was calculated without considering any loss; it is nearly four times greater than the value obtained from a 1kW system of 4 Sinergo solar batteries [18]. This is due not only to the fact that the plates of the Sinergo batteries are fixedly mounted at 15° angle to the horizon, but also that in practice it is possible to convert no more than 20 % of the energy of solar radiation [5]–[9], [18]. In reality, under the climatic conditions of Riga it is possible to obtain an average of 191 kWh of energy a year from solar radiation per $1m^2$ of horizontal surface.

The dynamics (character) of changes in the intensity of solar radiation measured in all considered cases shows that 85 % of the energy obtained by converting solar radiation is produced within 7 months (from March to September). But during the heating season from October to March, the potential of solar energy is negligible and cannot ensure even heating. Increasing the number of panels is not economical or is limited by the size of the roof. As a complement, it is possible to use the energy of the wind, the speed of which increases in autumn and winter (Fig. 2 b, c).

1.2 Evaluation of the Wind Resource

Using the results of measurements of wind speed, we evaluate the potential of the wind. The average speed is equal to 1.13 m/s, but sometimes the wind speed reaches (4÷5) m/s and more. The measurement results beginning from April 2013 showed that for almost half of the time (48 %) the wind speed was less than 1 m/s. Yearly average, 33 % of the time in Riga the value of the wind speed varies in the range of (1÷2) m/s, 12 % — (2÷3) m/s, 4 % — (3÷4) m/s, 2 % — more than 4 m/s. However, since the power of the wind turbine is proportional to the third power of the speed, even for a very short period of time it is possible to obtain a sufficient amount of energy.

It is known that the maximum available wind power is limited by C_{BZh} that is "the limit of Betz-Zhukovsky", which determines the ideal (without considering any losses) efficiency of wind turbines [19]–[20]. Ideally, it is possible to use only 59.3 % of the kinetic energy of the wind, as the maintenance of the air flow is required for any wind machine. This owes to the fact that, if the energy supplied by the wind is completely converted into useful work in the turbine, the output speed of the wind must be zero, i.e. a fresh wind flow cannot get into the turbine. For the wind to continue to move through the turbine, it is necessary for it to move inside turbine itself. Therefore, the efficiency of an ideal wind turbine of any design is defined by the limit $S_{BZh}= 16/27=0.59$ [19].

In [20] when deriving the formula for the calculation of the wind maximum available power it is taken into account through the wind energy use coefficient (WEUC) ξ ($\xi_{lim} \cong 0.59$). Modern wind turbines have a power factor ξ close to this limit, but as a rule their efficiency varies in the range of $0.2 \le \xi \le 0.40$. In our calculations of energy W_r, which can be obtained through the conversion of wind energy, we accept ξ_r=25 %. The calculation of the wind energy converted by the wind turbine with the wind wheel of $1m^2$, depending on the wind speed is shown in Table 3.

Table 3

Dependence of the Converted Energy on the Wind Speed

Velocity, m/s	Time, %	W_t, kW*h	W_r, kW*h
(0–1) m/s	49	31	
(1–2) m/s	33	311	93
(2–3) m/s	12	491	147
(3–4) m/s	4	440	132
(4–5) m/s and more	2	464	139
Total	100	1707	512

The energy W_t = 1707 kW·h is the total estimated energy that can be obtained during a year for the perfect wind turbine, taking into account the limit of Betz-Zhukovsky. But in practice, it $W_r = \xi_r \times W_t$ = 512kW*h can only be obtained per year. The diagram (Fig. 5) shows the amount of energy that can be obtained in practice at different wind speeds.

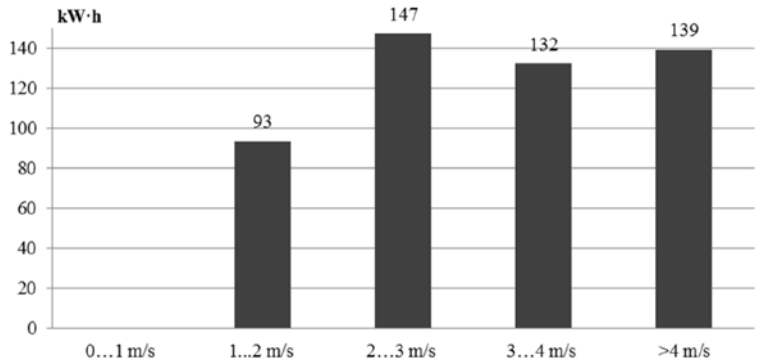

Fig. 5. The amount of converted wind energy W_r per year depending on the wind speed (see Table 3).

The calculations show that the amount of energy produced at speeds greater than 4 m/s, although the wind blows for much less time (6 times less), is comparable or even greater than the amount of energy obtained at a low speed of (1–2) m/s. It should be noted that the value of W_r per year was calculated taking into account that 49 % of the time the wind speed was less than 1 m/s (less than the start-up speed), at which even the most modern wind turbines do not run, including that of sail-type [19]–[21].

5. CONCLUSION

The analysis of the wind energy and solar radiation potential on the basis of measurements in Riga shows some promise for the development and implementation of various technologies, using these types of renewable energy sources, especially since on the market there are new technologies and combined systems for efficient conversion of renewable energy sources at low wind speeds and low levels of solar radiation to produce electricity, heating and water heating.

The potential of solar energy in Latvia is low, but it is comparable with many

European countries, where solar panels are widely used. The practice of known companies shows that for the production of electricity, solar radiation is used rather than heat. Therefore, regardless of the air temperature, solar batteries can perform their functions even in the winter sunny days when the air temperature can be -20 °C or lower.

Despite the fact that according to the results of the measurements, the average wind speed is low in Riga as well as in the ¾ part of the territory of Latvia, the calculations showed a real opportunity to obtain useful energy. In urban areas, it is possible to use small wind turbines of sail-type with a start-up speed of 1 m/s that can efficiently convert the energy of low-speed wind.

The analysis showed that during the heating season (6 months from October to March) the amount of solar radiation was 5 times less than during 6 months in summer and spring (Fig. 4). At the same time, on the contrary, increase in the wind speed during the cold season (see Fig. 2) made it possible to obtain 3.5 times greater amount of power than in the spring and summer. In general, combining devices for converting wind speed and solar radiation energy, 703 kWh of energy can be obtained per 1 m^2 of area in the climatic conditions typical of the most parts of Latvia. At the initial stage, it will require some financial investment, but in the future, it will not only reduce harmful emissions into the atmosphere, but also reduce the cost of electricity production. This is especially important for residential and commercial facilities, remote from centralised power lines, and in case of independent power supply of houses and buildings.

ACKNOWLEDGEMENTS

The present research has been conducted with financial support of the European Social Fund; the project has been implemented by the University of Latvia, No. 2013/0027/1DP/1.1.1.2.0/13/APIA/VIAA/007.

REFERENCES

1. Sievers, J., Faulstich, S., Puchta, M., Stadler, I., & Schmid, J. (2007). *Long-term perspectives for balancing fluctuating renewable energy sources*. Kassel, Germany: University of Kassel, Department of Efficient Energy Conversion. Available at http://desire.iwes.fraunhofer.de/files/deliverables/del_2.3.pdf
2. *Environment and Renewable Energy Industry in Latvia*. (2013). Available at http://www.liaa.gov.lv/files/liaa/attachments/k_2013environment_ and_ renewable_energy_ industry_in_latvia.pdf
3. Lukutin, B., Surzhikova, O., & Shandarova, E. (2008). *Vozobnovlyayemaya energetika v detsentralizovannom elektrosnabzhenii [Renewable energy in decentralized power supply]*. Moscow: Energoatomizdat
4. Goran Wall, M. (2014). Life cycle exergy analysis of solar energy systems. *J Fundam Renewable Energy Appl.*, *05*(01). doi:10.4172/2090-4541.1000146.
5. Alpicair. (2015). *AlpicAir gaiss-gaiss siltumsūkņi, zemes ūdens siltumsūkņi un saules kolektori [AlpicAir air-to-air heat pumps, ground water heat pumps and solar collectors]*. Available at http://alpicair.lv

6. *Tipy solnechnykh batarey i ikh KPD [Types of solar panels and their efficiency]*. (2015). Available at http://utem.org.ua/materials/show/%20tipy_solnechnyh
7. *Al'ternativnaya energiya. Solnechnaya energetika [Alternative energy. Solar power]*. (2015). Available at http://alternativenergy.ru/solnechnaya-energetika/
8. MIEL Group. (2015). *"Sun Republic" v Latvii poluchil grant Yevrosoyuza ["Sun Republic" received a grant from the European Union in Latvia]*. Available at http://www.miel.ru/lenta/3486/
9. *Sailessūknis. Solārās apkures sistēma [Saulessuknis. A solar heating system]*. (2015). Available at http://saulessuknis.lv
10. Bezrukovs, V., Bezrukovs, V., Zacepins, A., & Komashilovs, V. (2015). Assessment of wind shear and wind energy potential in the Baltic Sea region of Latvia. *Latvian Journal of Physics and Technical Sciences*, *52*(2), 26–39. doi:10.1515/lpts-2015-0009
11. Lizuma, L., Avotniece, Z., Rupainis, S., & Teilans, A. (2013). Assessment of the present and future offshore wind power potential: a case study in a target territory of the Baltic Sea near the Latvian coast. *The Scientific World Journal*, *2013*, 1–10. doi:10.1155/2013/126428
12. Rolik, Y., & Gornostay, A. (2015). Analiz osnovnykh ekonomicheskikh pokazateley raboty vetroustanovok po rezul'tatam opyta kommercheskoy ekspluatatsii vetroparkov Latvii [Analysis of the major economic factors of the wind turbines performance based on the results of commercial service experience of the wind-farms in Latvia]. *Izvestiya vysshikh uchebnykh zavedeniy i energeticheskikh ob"yedineniy SNG. Energetika [News of higher educational institutions and the energy association in CIS countries. Energetics]*, *2*, 88–94. Available at http://rep.bntu.by/handle/data/17335
13. EEM. (2015). *Energoefektivitātes monitorings [Energy efficiency monitoring]*. Available at http://www.eem.lv
14. *Laboratory for Mathematical Modelling of Environmental and Technological Processes*. (2015). Available at http://www.modlab.lv
15. Latvian Environment, Geology and Meteorology Centre. (2015). *Operational Information*. Available at http://www.meteo.lv/en/meteorologijas-operativa-informacija/
16. Regulations of the Cabinet of Ministers of the Republic of Latvia. (2015). *Latvian Construction Standards LBN 003-01"Construction Climatology"*
17. Photovoltaic Geographical Information System. (2015). *PV Potential Estimation Utility*. Available at http://re.jrc.ec.europa.eu/pvgis/apps4/pvest.php
18. Sinergo. (2015). *Saules bateriju sistēmas darbības tiešsaiste [Solar system operation online]*. Available at http://sinergo.lv/1kw-system-online/
19. Hansen, M. (2008). *Aerodynamics of Wind Turbines*. London: Earthscan.
20. Sakipova, S., & Jakovics, A. (2014). Sail-type wind turbine for autonomous power supply: Possible use in Latvia. *Latvian Journal of Physics and Technical Sciences*, *51*(6), 13–25. doi:10.1515/lpts-2014-0033
21. Sakipova, S., Jakovics, A., Gendelis, S., Kambarova, Z., & Kussaiynov, Y. (2014). Development of a sail type wind turbine for autonomous energy supply according to climate conditions. *Eurasian Physical Technical Journal*, *11*(2), 11–19

ATJAUNOJAMO ENERGORESURSU POTENCIĀLS LATVIJĀ

S. Sakipova, A. Jakovičs, S. Gendelis, E. A. Buketov

K o p s a v i l k u m s

Pētījumā tiek analizētas atjaunojamo enerģijas avotu izmantošanas iespējas Latvijas klimatiskajos apstākļos ar salīdzinoši zemu raksturīgo vēja ātrumu un nelielu saulaino dienu skaitu gadā. Darbā vispirms raksturotas mērierīces, ar kurām tiek veikti apkārtējās vides parametru - vēja ātruma un virziena, gaisa temperatūras un solārā starojuma mērījumi. Pamatojoties uz pēdējo divu gadu meteoroloģiskajiem datiem, tiek analizēts vēja un saules starojuma enerģijas potenciāls un ir novērtēts arī reāli saražojamās enerģijas daudzums, kas parāda, ka stabilam energonodrošinājumam šos atjaunojamos enerģijas avotus praksē nepieciešams kombinēt ar citiem.

20.08.2015.

LATVIAN JOURNAL OF PHYSICS AND TECHNICAL SCIENCES
2016, N 1

DOI: 10.1515/lpts-2016-0002

DEVELOPMENT OF POWER SUPPLY MANAGEMENT MODULE FOR RADIO SIGNAL REPEATERS OF AUTOMATIC METERING READING SYSTEM IN VARIABLE SOLAR DENSITY CONDITIONS

K. Kondratjevs[1], A. Zabasta[2], V. Selmanovs-Pless[3]

[1]Riga Technical University, Faculty of Power and Electrical Engineering, Institute of Industrial Electronics and Electrical Engineering,
12/1 Azenes Str., Riga, LV-1048, LATVIA
[2,3] Mazzy Ltd, Riga, 3 Balasta dambis, LV-1048, LATVIA
e-mail: Anatolijs.Zabasta@gmail.com

In recent years, there has been significant research focus that revolves around harvesting and minimising energy consumption by wireless sensor network nodes. When a sensor node is depleted of energy, it becomes unresponsive and disconnected from the network that can significantly influence the performance of the whole network. The purpose of the present research is to create a power supply management module in order to provide stable operating voltage for autonomous operations of radio signal repeaters, sensors or gateways of WSN. The developed management module is composed of a solar panel, lithium battery and power supply management module. The novelty of the research is the management module, which ensures stable and uninterrupted operations of electronic equipment in various power supply modes in different situations, simultaneously ensuring energy protection and sustainability of the module components. The management module is able to provide power supply of 5 V for electronics scheme independently, without power interruption switching between power sources and power flows in different directions.

Keywords: *power supply, power supply management, smart meters, wireless sensor networks.*

1. INTRODUCTION

Energy usage is a very important concern in wireless sensor networks (WSNs) taking into account that sensor nodes and other WSN elements often operate on limited battery power. In recent years, there has been significant research focus that revolves around harvesting and minimising energy. When a sensor node is depleted of energy, it will die and disconnect from the network, which can significantly influence the performance of the application. Sensor network lifetime depends on the number of active nodes and connectivity of the network, so energy must be used efficiently in order to maximise the network lifetime. Therefore, research on energy management and sustainability is conducted in different directions.

Hence, power conservation and power management take on additional importance. It is for these reasons that researchers are currently focusing on the design of

power-aware protocols and algorithms for sensor networks [1].

An example could be a solution applied to the project WSN for water distribution networks in Talsi, Latvia [2]. The sensors of the system have only two regimes: registration of impulses from water meters and transmission of telegrams several times per hour; therefore, synchronization is not used for network sensors. The power consumption of the sensors / transmitters is estimated for at least 10 years of operation time without battery replacement in case of operating regime, when messages are transmitted each 30 minutes. Such operation lifetime is achieved owing to 7500–8000 mAh battery and economical regime of transmitter [2].

According to research [3], energy harvesting involves nodes replenishing their energy from an energy source. Potential energy sources include solar cells [4], vibration, fuel cells, acoustic noise, and mobile supplier. In terms of harvesting energy from the environment [5], a solar cell is the current mature technique that harvests energy from light. There is also a study on the use of a mobile energy supplier such as a robot to replenish energy. The robots would be responsible for charging themselves with energy and then delivering energy to the nodes [3].

Harvesting energy from the environment is feasible in many applications to ameliorate the energy limitations in sensor networks. For example, in paper [4], an adaptive duty-cycling algorithm is presented that allows energy harvesting sensor nodes to autonomously adjust their duty cycle according to the energy availability in the environment. The algorithm has three objectives, namely, achieving energy neutral operation, i.e., energy consumption should not be more than the energy provided by the environment; maximising the system performance based on an application utility model subject to the above energy-neutrality constraint; and adapting to the dynamics of the energy source at run-time.

Another important thing is the ability to run from low power levels. Only smart electricity meters have the luxury to have a grid power source and, even in this case, consumption must be minimised as the power to run the devices comes from the utility and not from the customer. Gas and water meters, on the other hand, need to be able to run from a battery, and guarantee a lifetime of ten years or more. This puts severe constraints on the efficiency of the power converter as well as the remaining meter electronics [6].

Furthermore, new types of meters need to be able to support 32-bit microprocessors and larger memory sizes so that they can provide cryptographic features, as well as more fine-grained usage measurements and data updates via wireless communications [6]. If external electrical power fails, the meter needs to be able to send notifications to the utility, demanding the use of backup energy strategies.

Gas and water meters place stringent demands on efficiency and use ultra-low-energy sleep modes to improve battery lifetime. For such applications, for example, TPS65290 device [7] for power-management of integrated circuits that can operate over a wide range of system load conditions ranging from fractions of microamperes to a few hundred milliamps can be used. This is a typical device used as Low Power, Energy Harvesting Systems. The device operates over a wide 2.2 V to 5 V input-voltage range and incorporates a very-low quiescent current, always-on power supply, a 500 mA buck/boost converter, a 150 mA low dropout regulator, and eight power-distribution switches to provide a high degree of power control to meter

electronics. One power switch can maintain the MCU in its sleep state, but cut power to analogue sensors while they are not being used.

The buck-boost converters can work in either PWM or pulse frequency modulation (PFM) modes, the latter being used for very light loads. The device can be configured to work in only PWM mode if output ripple is an issue.

There is also the risk that the battery in a gas or water meter may fail early. Therefore, a backup energy source is needed. Although one option is to use a rechargeable battery, this necessitates the use of a charging circuit to maintain the battery at peak charge for use only in comparatively rare situations. Furthermore, the key requirement is for an instantaneously available backup source that will work at the low temperatures needed for outdoor units. The meter can then immediately transmit status information to the remote hub that collects usage data and alerts.

An effective alternative to a battery is to use a double-layer capacitor or "supercapacitor". This is relatively straightforward to integrate into a circuit because it has the ability to store enough energy to maintain the basic functions of a smart meter temporarily without demanding complex switching logic [8]. However, the application of double-layer capacitors in WSN networks now is rather theoretical than practical.

The purpose of the research is to create a power supply management module in order to provide 5 V operating voltage for autonomous operations of radio signal repeaters, sensors or gateways of WSN. The power supply management module is composed of electronic circuits – signal repeater energy source – solar panel storage solution – battery and power management module.

At present, the world's existing solutions operate by the principle of the foundation, i.e. the scheme when the power is supplied from two sources: "core" and "reserves", and energy to the load is supplied through the unifying schema either from a basic source or from a reserve one. However, fully stable and autonomous power development is a complex process due to the proper selection of components, calibration, and so on.

Therefore, the novelty of the research is to design and test the management module, which ensures stable and uninterrupted operations of electronic equipment in various power supply modes in different situations, simultaneously ensuring energy protection and sustainability of the module components.

It is noted that the single power source unit is solar panels; electric storage type is a lithium battery or equivalent. It is a minimised solution of self-discharge under normal operating conditions, and it allows minimising degradation of all elements over time. It is possible to provide uninterrupted power supply of 5 V for electronics scheme independently, without power interruption switching between power sources and power flows in different directions.

2. POWER SUPPLY MANAGEMENT MODULE DEVELOPMENT

The research was conducted within the framework of the project "Photovoltaic Module Energy Storage and Management Studies Autonomous Electronics – Repeater Development" in 2014–15.

The task of the developed photovoltaic power system is to ensure a sufficient working cycle for collecting metering data from a distributed sensor nodes by receiving or repeating sensor-metering telegrams. These telegrams contain temperature, pressure, moisture, electricity and water usage information. The examples of the wireless network sensors tested for the photovoltaic power system within the framework of the project can be seen in Fig. 1.

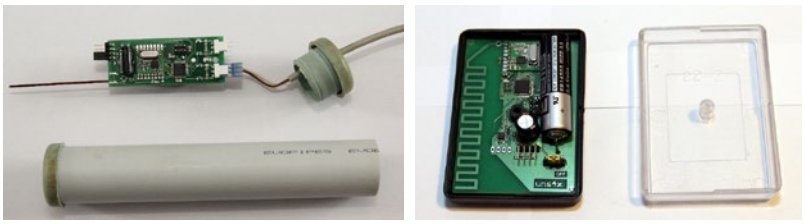

Fig. 1. Water flow (on the left) and moisture (on the right) wireless sensor devices.

To increase the efficiency of a solar panel, Maximum Power Point Tracking (MPPT) is applied. The purpose is to maximise the power output of a selected photovoltaic module by varying the current to the load and battery charging.

The proposed solution consists of two types of solar battery charging circuits suitable for solar power applications in smart metering applications that is able to provide uninterrupted power supply of 5 V for electronics scheme independently, without power interruption switching between power sources and power flows in different directions.

The research was conducted in two stages: the first prototype was developed and tested, then after improvement and additional function adding the second prototyped was created.

A. The First Prototype Development

The purpose of the first prototype is to charge the battery attached to a power sensor, repeater or gateway devices. During dark hours, the stored energy of the battery is used to extend the uptime of the connected equipment. Up to four independent solar cell modules can be connected to the module.

The choice of the solar panel is critical and has to be calculated for the work-operating mode of the connected equipment. The work-operating mode of the connected equipment has to adapt to the charge level of the selected battery and work cycles controlled in combination with microcontroller sleep times.

The module consists of:

- Several uniting diodes for multiple concurrent solar panel connections;
- Step down impulse converter;
- Lithium battery charging controller;
- Battery wrong connection protection (polyfuse);
- Circuit for uninterrupted switchover from the solar panel power to the battery and vice versa.

Uniting diodes

- Make it possible to increase power by connecting additional panels;
- Make it possible to simultaneously use multiple panels toward the sun oriented in different directions.

Step-down impulse converter

LM22675 controller [9] with operating frequency of 500 kHz allows the inductor to reduce the cumulative nominal and dimensions. It operates in pulse mode with the internal circuit-breakers transistor up to 1.8 A per pulse. Resistors R1 and R2 form a divider to compare the output voltage with the reference voltage of 1.28 V. When a voltage is higher than the reference voltage, the regulator reduces the internal power MOSFET transistor open interval, but when a voltage is smaller, it increases the interval. In an open state, the current is accumulated in inductor L1, but in a closed state, the inductor energy is transferred through the diode to capacitor C5. The filter capacitors C6 and C7 are for operational stability. The selected output voltage of 5 V is adapted for the electronic equipment in the particular application.

Lithium battery charging controller

Universal lithium battery charger controller with a fully charged battery nominal voltage of 4.23V. The controller provides the programmed charging current until the nominal voltage current is reached – after that the charging is switched off with a corresponding reduction in current. Charging current is assigned with resistor R3 in correspondence with the measurement of selected solar panel.

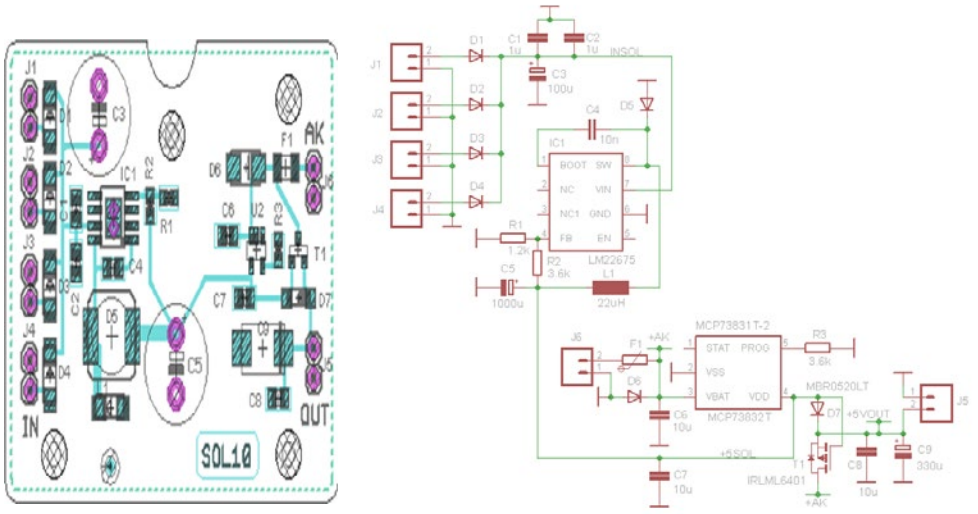

Fig. 2. Electrical and montage schemes of photovoltaic power system module, the 1st prototype.

Battery wrong connection protection

Polyfuse F1 and diode D6 protect the board and the battery in case of incorrect polarity mismatch. The board returns to a normal work mode after the battery is connected correctly.

Circuit for uninterrupted switchover from solar panel power to a battery and vice versa

The scheme consists of diode D7 and transistor T1. Scheme could be built with two diodes, but to reduce the voltage loss during switching on the battery-feeding mode, a MOSFET transistor with a very low resistance in the open state is used. Transistor resistance constitutes just small portion of Ohm – up to 0.05 Ω at high currents. The drop on the diode should be around 0.5 V.

B. The Second Prototype Development and Improvements

The second prototype ensures the charging of a battery and provision of power to the connected equipment by optimising the solar panel maximum possible power rate at variable lightning conditions (see Fig. 3).

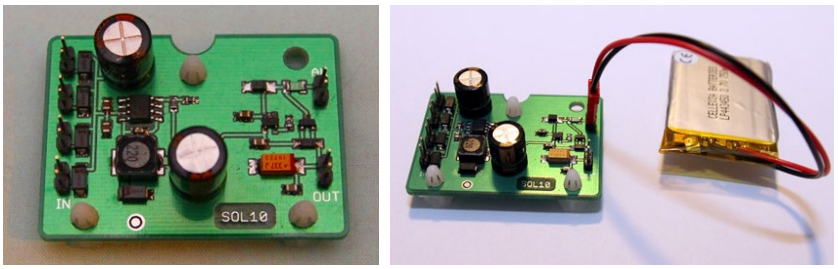

Fig. 3. The appearance of photovoltaic power system module, the 2nd prototype.

The varying maximum solar panel voltages and supplied maximum power are used to ensure maximized usage time of the connected application.

The board consists of such components (see Figs. 4 and 5):

- Uniting diodes to connect multiple solar panels at the same time;
- Step-down impulse converter;
- Lithium battery charging circuit (exchangeable with alternate if the battery type varies);
- Battery wrong connection protection (polyfuse);
- Circuit for uninterrupted switchover from solar panel power to the battery and vice versa;
- Digital potentiometer and ADC;
- Load disconnection circuit;
- Microcontroller;
- Microcontroller software – control algorithm.

Improved photovoltaic power system enables the battery charging current control and adjusts optimal working point of solar cells (MPPT); therefore, the used power is the maximum provided by the solar panels.

In order to save place the authors do not describe such components of the power supply management module as *uniting diodes, step-down impulse converter, lithium battery charging controller, battery wrong connection protection, circuit for uninterrupted switchover from solar panel power to battery and vice versa*. These components have been described in Section A “The First Prototype Development”.

Therefore, only the description of additional components is provided further.

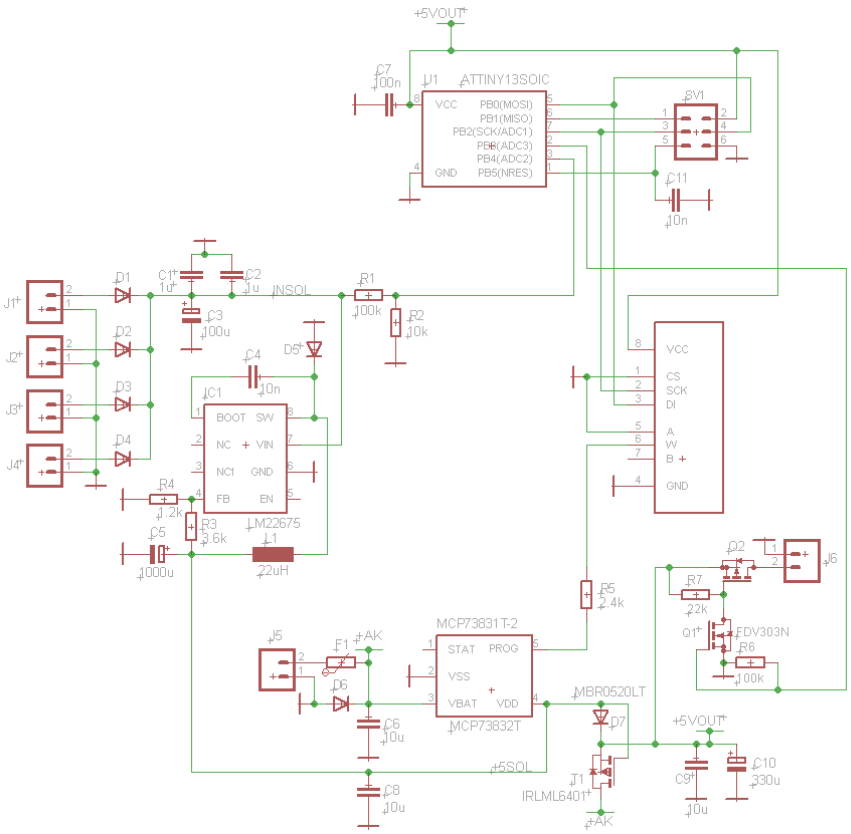

Fig. 4. Electrical schemes of photovoltaic power system module, the 2nd prototype.

Digital potentiometer

The digital potentiometer together with resistor R5 enables the controllers to change the battery charging current and adjusts their optimal working point of solar cells (MPPT) – the used power is the maximum provided by the solar panels. If the digital potentiometer mode is zero, then only the resistor R5 limits the maximum charging current. When the potentiometer is switched on, the charging current decreases. The microcontroller ATTINY13A controls the potentiometer. An essential element of the module is the ADC that is implemented on ATTINY13A pin ADC2. Resistor divider aligns the input voltage from the solar panels to the ADC reference voltage and enables the management software to read the maximum power point and adjust the charging current.

Load disconnection circuit

When it is necessary to shut off the load from the battery, in case of deep discharge or other reasons, the transistors Q1 and Q2 operate and disconnect the load using the signal line from the microcontroller. In other cases, the transistor Q2 is permanently open and connects the load to the power source.

Microcontroller

The task of microcontroller implemented on ATTINY13A is to combine the

solar panel voltage measurements with ADC, to drive the digital potentiometer by ensuring the optimal charging current selection and to control the load disconnection and connection. The interface of the digital potentiometer is SPI where the pin number 8 of the microcontroller is used.

Microcontroller software – control algorithm

The control software is modular: ADC, digital potentiometer driver, disconnection module and logical machine algorithm. ADC measured input voltage of the solar panel for the selected panel is in the range up to 20 V. The divisor reduces the voltage to a reference voltage and the software finds the current voltage value. This voltage is the starting point for the determination of the optimal power point for the selected solar panel. This point must be observed by monitoring the nominal voltage drops and adapting the charging current. If the voltage does not decrease, the charging current can be the maximum provided by the solar panel. Connected equipment should be designed to be able to cope with power supply disconnection in cases when a battery approaching to discharge or the light intensity becomes too weak.

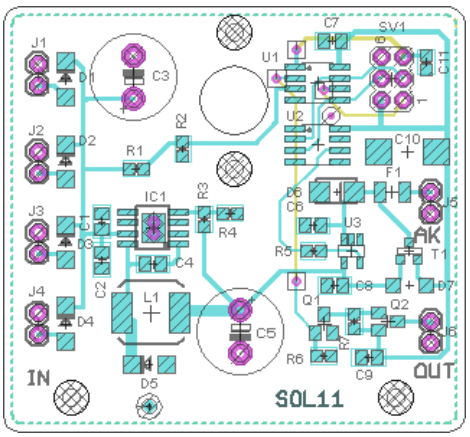

Fig. 5. Montage schemes of photovoltaic power system module, the 2nd prototype.

3. CONCLUSIONS

The aim of the present research has been to create the power supply management module in order to provide stable operating voltage for autonomous operations of radio signal repeaters, sensors or gateways of WSN. The research has been conducted in two stages: the first prototype has been developed and tested, then after improvement and additional function adding, the second prototype has been developed. The second prototype ensures the charging of a battery and provides power to the connected equipment by optimising the solar panel maximum possible power rate under variable lightning conditions.

The developed management module is composed of solar panel storage solution, lithium battery or equivalent and power management module. The novelty of the research is the management module, which ensures stable and uninterrupted operations of electronic equipment in various power supply modes in different situations, simultaneously ensuring energy protection and sustainability of the module

components. The management model can provide uninterrupted power supply of 5 V for electronics scheme independently, without power interruption switching between power sources and power flows in different directions.

ACKNOWLEDGEMENTS

Support for the present research has been provided by the Research project NR.1.21 "Photovoltaic Module Energy Storage and Management Studies Autonomous Electronics – Repeater Development" (Contract No. L-KC-11-0006 Project No. KC / 2.1.2.1.1 / 10/01/005).

REFERENCES

1. Akyildiz, I. F., Su, W., Sankarasubramaniam, Y., and Cayirci, E. (2002). Wireless sensor networks: A survey. *Computer Networks* 38, 393–422.
2. Zabasta, A., Kunicina, N., Chaiko, Y., and Ribickis, L. Automatic meters reading for water distribution network in Talsi City. In *Proceedings of EUROCON 2011*, 27–29 April 2011, Lisbon, Portugal, IEEE, Instituto Superior Tecnico, Instituto de Telecomunicacoes, (pp. 1–4).
3. Yick, J., Mukherjee, B., and Ghosal, D. (2008). Wireless sensor network survey. *Computer Networks* 52, 2292–2330.
4. Kansai, A., and Srivastava, M.B. (2003). An environmental energy harvesting framework for sensor networks. In *Proceedings of the International Symposium on Low Power Electronics and Design* (pp. 180–185).
5. Raghunathan, V., Kansai, A., Hse, J., Friedman, J., and Srivastava, M. (2005). Design considerations for solar energy harvesting wireless embedded systems. In *Proceedings of the IPSN*, 457–462.
6. *Power Supply Design for Smart Meters*. (2013). Publitek Marketing Communications 2013-10-22. Available at http://www.digikey.com/en/articles/techzone/2013/oct/power-supply-design-for-smart-meters.
7. *Low Quiescent Current, Multi-Mode PMIC for Battery Powered, Energy-Harvesting Applications*. (2013). Texas Instruments, SLVSBY5B. Available at http://www.ti.com/lit/ds/symlink/tps65290.pdf.
8. Zhang, J., Zhang, L., Liu, H., Sun, A., and Liu, R. (2012). *Electrochemical Technologies for Energy Storage and Conversion*. John Wiley & Sons, Technology & Engineering.
9. Simpson, C. (2011). *Battery Charging*, LM2576, LM3420, LP2951, LP2952, Texas Instruments, Literature Number: SNVA557, pp. 1–19.

ELEKTROAPGĀDES VADĪBAS MODUĻA IZSTRĀDE RADIO SIGNĀLU RETRANSLATORIEM, KAS DARBOJAS AUTOMATIZĒTĀ MĒRĪŠANAS NOLASĪŠANAS SISTĒMĀ MAINĪGOS SAULES RADIĀCIJAS APSTĀKĻOS

K. Kondratjevs, A.Zabašta, V. Šelmanovs-Plešs.

K o p s a v i l k u m s

Pēdējos gados vairāki pētījumi ir veltīti problēmām, kas ir saistītas ar enerģijas patēriņa mazināšanu un efektīvu izmantošanu bezvadu sensoru tīklu mezglos. Kad sensors mezgls ir izsmēlis enerģijas krājumu, tas vairs nefunkcionē un atslēdzas no kopēja tīkla, kas var būtiski ietekmēt visa tīkla veiktspēju.

Šī pētījuma mērķis ir izveidot barošanas vadības moduli, lai nodrošinātu stabilu elektroapgādes spriegumu autonomi strādājošiem radio signāla atkārtotājiem, sensoriem vai vārtejām, kas darbojas bezvadu sensoru tīklos. Izstrādātais vadības modulis sastāv no saules paneļu fotoelementu moduļa, uzglabāšanas risinājuma (litija vai līdzvērtīgas baterijas) un elektroapgādes pārvaldības moduļa.

Pētījuma novitāte ir elektroapgādes pārvaldības modulis, kas nodrošina stabilu un nepārtrauktu elektroniskas iekārtas darbību dažādos barošanas režīmos, dažādās situācijās, vienlaikus nodrošinot enerģijas aizsardzību un moduļa sastāvdaļu ilgtspēju. Izstrādātais risinājums nodrošina nepārtrauktu 5V barošanu elektronikas shēmām bez strāvas pārtraukuma, kad notiek komutācijas starp barošanas avotiem un enerģijas plūsmām dažādos virzienos. Elektroapgādes pārvaldības modulis nodrošina stabilu spriegumu mainīgos saules radiācijas apstākļos.

27.10. 2015.

LATVIAN JOURNAL OF PHYSICS AND TECHNICAL SCIENCES
2016, N 1

DOI: 10.1515/lpts-2016-0003

SMOOTH TRACKING TRAJECTORY GENERATION OF LARGE ANTENNA

S. Upnere*, N. Jekabsons, U. Locans

Ventspils University College,
101 Inženieru Str., Ventspils, LV – 3601, LATVIA
*Corresponding author: sabineu@venta.lv

The current paper presents an engineering approach for studies of the control algorithm designed for a mechanically robust large antenna. Feed-forward control methods with the 3rd-order polynomial tracking algorithm are supplemented to the original feed-back PID control system. Dynamical model of the existing servo system of 32m radio telescope has been developed to widen a case analysis of observation sessions and efficiency of the control algorithms due to limited access to an antenna. Algorithms along with the results from the system implemented on a real antenna as well as model results are presented.

Keywords: *dynamical model, path planning, PID controller, tracking algorithm.*

1. INTRODUCTION

The control systems of antennas and telescopes ensure accurate pointing (reaching the target object) and tracking (following the object during its apparent motion). Pointing and tracking are constrained by existing technical parameters of the drive system and mechanical properties of the whole construction (such as maximum motor torque, system acceleration and velocity), as well as by the choice of antenna control algorithms. Resultant accuracy and agility of a pointing and tracking system often limit the performance of the antenna.

There are several algorithms available that provide the control of antennas and telescopes. Proportional-Integral (PI) and Proportional-Integral-Derivative (PID) controller can be regarded as a classical approach in the antenna industry [1]. Over the last decades, a number of PID design methods have been proposed [2], [3], [4]. For PID controllers, windup is a characteristic feature; therefore, several anti-windup controller design methods have been proposed to suppress windup degradation ([5], [6], [7]).

Model-based design methods are often employed by control engineers and researchers. There have been several studies of model-based controllers applicable to the control system of the antenna and telescope, such as linear-quadratic-Gaussian [8] or H∞ controller [9]. Gawronski and Souccar have performed the analysis of the

effectiveness of different controller combinations in one system [1].

The transient response of a practical control system with a plant often exhibits damped oscillations before reaching a steady state [3]. One of transient response characteristics is settling time. It is the time required for a response curve to reach and stay within a range about the final value of size specified by absolute percentage of the final value [3]. There are references available which describe various approaches how to reduce overshoots before reaching a steady state. For example, one can change controller coefficients [10] or change planning of movement trajectory using the 5th-order polynomial [11] or the 3rd-order polynomial [12].

In general, there are two options that improve the efficiency of a tracking algorithm: feed-forward control and feed-back corrections. In this paper, we present the combined approach using the 3rd-order trajectory generation algorithm and PID controller to advance antenna switching between sources during the observation session. The objective of this study is the development of an additional feed-forward algorithm for existing PID controller of the antenna in terms of requirements for high accuracy observations and without changes in hardware. The used algorithm provides the desired position, velocity and acceleration limits, permitting their use in control to improve the tracking accuracy at all points on the path.

In order to check a tracking algorithm, the radio telescope RT-32 of Ventspils International Radio Astronomy Centre (VIRAC) located in Irbene (Latvia) has been used. The dish size of the fully steerable radio telescope RT-32 is 32 meters. Several experiments with different control algorithms have been performed using RT-32. However, real observations are a rather slow process; thus, this approach somehow limits a feasible number of pointing and tracking scenarios for controller evaluation. Thus, additional models of RT-32 servo system have been developed. Mechanical and kinematic models of existing RT-32 drive system have been used for optimal movement planning during the Very Long Baseline Interferometry (VLBI) sessions or satellite tracking. Experimental measurements have been performed by tracking multiple objects.

2. RADIO TELESCOPE RT-32

The key applications of RT-32 are VLBI observations of ionosphere, participation in the European VLBI Network (EVN), radar-VLBI (investigation of radio-silent near-space objects, such as cosmic debris, asteroids), and single-dish solar observations. This kind of usage defines strict requirements for the whole drive system, mainly due to needs of fast switching between observational objects and accurate tracking of relatively fast objects.

RT-32 can rotate around azimuth (vertical) and altitude (horizontal) axes. Two motors drive the azimuth axis and the other two motors move the altitude axis. All the motors are driven in the current mode with the aid of electro-mechanical amplifiers. Angular positions on the both axes are measured using rotary encoders, angular velocities – with tachometers. Simplified telescope scheme is illustrated in Fig 1.

The main frequency range of the telescope is 1 – 12GHz. For this study, 5 GHz frequency has been used; therefore, RT-32 beam width is 7.8 arcmin. It has

been assumed that the antenna "sees" an observational object if it is at least 4 arcmin from the target, and that the antenna must be on track for at least 20 seconds in order to have viable output from the correlation software.

Technologically, the pointing accuracy of the RT-32 antenna is strictly limited to 20 arc sec, mainly due to a digital sampling error of the optical angular encoders from the period of 1960–1980. At the moment of paper submission, a large-scale renovation of RT-32 is taking place at VIRAC. After renovation in 2015, new azimuth sensors have specification of nominal resolution of »1.2 arc sec.

However, as it follows from the practice, the total pointing error usually reaches much higher values. Analysis of recent observation sessions (2008–2014) indicates that tracking accuracy is often limited by settling time, which for the existing RT-32 antenna drive system can reach ≈40 s and even more. These oscillations mainly happen during the target switching when the dish slows down from the "highway" angular velocities of approximately »10 deg/min to much slower pace of celestial bodies. The amplitude of these prolonged oscillations can be large enough to disturb the observation session – in fact settlement oscillations of the main mirror may disable VLBI observations for up to 70 % of total targets of EVN sessions. More targets could be tracked by suppression of oscillations after target switching.

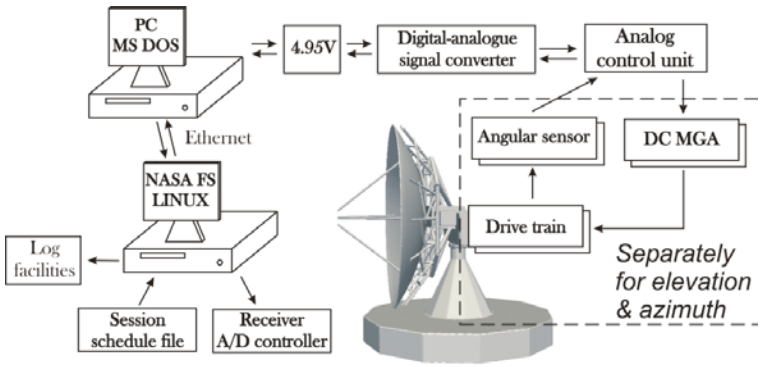

Fig. 1. Simplified scheme of RT-32 (in 2014), where NASA FS is NASA Field System, DC MGA is DC motor-generator amplifier.

2.1. Control System of RT-32

The radio telescope RT-32 is controlled by a PID controller. Such controllers are widely used in the antenna and radio telescope industry. The controller can be expressed mathematically as [4]:

$$u(t) = k_p e(t) + k_i \int_0^t e(\tau)\, d\tau + k_d \frac{de(t)}{dt}, \quad (1)$$

where *u(t)* is input signal of the plant (manipulated variable), *e(t)* is error signal defined as $e(t)=r(t)-y(t)$, *r(t)* is reference input signal, k_p is controller gain, k_i is integral gain and k_d is derivative gain. The process variables *y(t)* are signals from angular encoders (in *e*) and tachometers (in *de/dt*).

To obtain an optimal set of parameters k_p, k_d, and k_i that will give a stable operation of the RT-32 system, manual controller tuning has been performed during Sun and satellite observations. These parameters may differ for the cases of tracking, pointing and controlled movements (like switching from one celestial body to another).

The AC converter imposes a threshold limit of output voltage $|u|=u_0$ (where $u_0=4.95\ V$ is a control voltage), which breaks linearity of Eq. (1).

There are three modes of operation (separately for each axis) in the PID controller depending on a distance from the target. If the antenna is more than 3 degrees away from a target, the antenna is moved with maximum possible velocity. When the antenna reaches 3 degrees from the object trajectory, the PID controller takes over, but the integral part of the PID controller is enabled only when the antenna is 0.25 degrees from the trajectory of a targeted object.

The principal problem related to this approach is poor settling performance after a large move (see Fig. 2(a)).The integral sum starts accumulating when the controller is first switched on and continues to change as long as a controller error exists. If there is a difference between the desired and measured values, the resulting error will cause a continuing increase in the integral term.

In our case, the suppression of the integral windup is implemented with the help of an additional algorithm (PID+AA), which calculates a new tracking trajectory of an antenna (see Fig. 2(b)). A modelled trajectory starts at the initial position of the antenna and finishes at some point on the trajectory of the target. We would like to speculate that the algorithm can reduce oscillations of the antenna, because when the antenna is in a position where the PID controller takes over, the antenna control is no longer correcting errors between the current position and the desired position. Instead, it is now correcting errors between the current position and the provided trajectory. Because of the minimal differences, this results in a smoother deceleration, when the antenna reaches its targeted position.

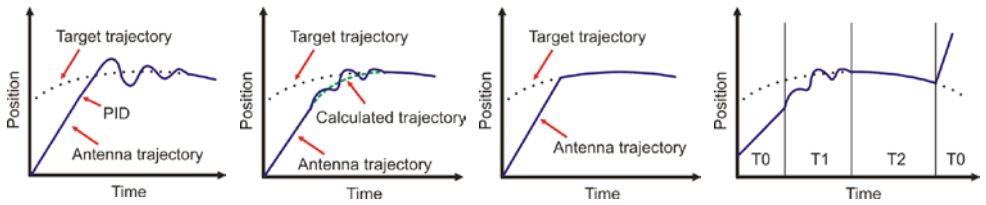

Fig. 2. Illustration of the initial RT-32 control (PID) with noteworthy oscillations (a); implemented approach for the suppression of the integral windup (b) using an additional algorithm (PID+AA); trajectory of an ideal plant and control (c). Time regions in target observation (d): the antenna moves at a maximum speed or acceleration, T0, the antenna reaches a target trajectory, T1, and the antenna tracks a target, T2.

We have assumed an ideal control and ideal plant which can move without any oscillations and immediately be on the trajectory when it is reached to get the qualitative estimation of algorithm efficiency (see Fig. 2(c)). Time and position when

the ideal system gets the target trajectory are defined using the maximum velocity of the antenna.

Observational time of a target can be divided into three time regions (see Fig. 2(d)): (1) a region where the antenna moves at a maximum speed or acceleration to reach a trajectory of the observational object, T0; (2) a region of corrections – pointing and settling time, T1; (3) a tracking region of a target, T2.

3. DYNAMICAL MODEL OF THE SERVO SYSTEM

To analyse fictive observation sessions and to study different control approaches and algorithms for antenna control, the dynamical model of RT-32 has been developed. Because of the RT-32 technical robustness (notable non-linearity and hysteresis of current amplifiers and engines, noisy encoders), it is a challenge to develop a dynamical model of this telescope servo system. The model which is in the acceptable agreement with the observed behaviour of RT-32 includes the drive system, second-order friction, and noise. Equations (2)–(3) describe the kinematics and dynamics of the model:

$$\dot{\alpha} = \int_{t_0}^{t_n} \ddot{\alpha} dt + \dot{\alpha_{t_0}}, \quad \alpha = \int_{t_0}^{t_n} \dot{\alpha} dt + \alpha_{t_0}, \tag{2}$$

where $\dot{\alpha} = \omega$, and

$$\dot{\omega} = \frac{M_0}{\omega_s}\left[u_{ref} - \omega_{ref} + \kappa\omega_{ref} - \kappa\omega_{ref}^2 + \lambda f_g\right], \tag{3}$$

where M_0 is torque constant, $u_{ref}=u/u_0$, u is voltage, $w_{ref}=\omega/w_s$, w_s is maximum angular velocity, ω is angular velocity, λ and κ are friction constants, and η is noise. Gear friction f_g is:

$$f_g = \frac{d}{dt}\int_0^t v(t-\tau)e^{-\tau/\tau_0}d\tau. \tag{4}$$

DC motor-generator amplifier (DC MGA) is part of the model. Experimentally measured DC MGA transfer curve is shown in Fig. 3.

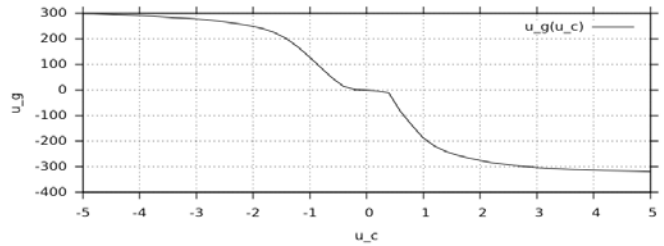

Fig. 3. Measured DC motor-generator amplifier transfer curve of the radio telescope RT-32.

The comparison of experimental and model values has shown that a magnetic hysteresis-like phenomenon has to be taken into account. The hysteresis is defined

by the following integral:

$$u_{mag} = \xi \int_0^t f(u_c, u_{mag}) \left|\frac{du_c}{d\tau}\right| d\tau, \tag{5}$$

where

$$f(u_c, u_{mag}) = \begin{cases} 0, if \ |u_c - u_{mag}| < 3.5 \\ 1, \ else \end{cases} \tag{6}$$

and u_c is voltage calculated by considering time delay and internal resistance of the system, ξ is a model constant.

4. POLYNOMIAL-BASED TRACKING ALGORITHM

The following happens in a standard VLBI tracking scenario. When a track command of RT-32 is called, the control system software uses an astronomical module to create a table, which describes the desired antenna position and the time when the antenna needs to be in the particular position to follow the body specified. The control algorithm then ensures the movement of the antenna between entries of a created table at a speed necessary to reach the next position described in this table. The algorithm automatically blends together subsequent moves so that the ending velocity and position of one move become the starting velocity and position for the next move.

To minimise the settling time introduced by the PID controller, a similar approach to [11] and [12] has been designed to move the antenna in a position to track objects.

During the study, a second-order polynomial has been inspected to define the antenna path in the hyperspace of two angles and time. However, in situations when the antenna's current position and targeted object position are very close and the antenna is moving slowly a second-order polynomial does not provide significant improvement. This can be explained by the fact that the tracking algorithm does not take the necessary acceleration of the antenna into account, when creating a trajectory for the desired object. For situations when antenna's motion is slow and the distance to the targeted object is small this results in trajectories that require antenna acceleration that exceeds system limitation.

Additional algorithm continuously checks the antenna position. When the antenna moves closer than 3 degrees from the source, it creates a trajectory using a third-order position polynomial (Eq. (7)), which the controller should employ for the antenna to reach its intended position.

$$x(t) = x_0 + \alpha\tau + \beta\tau^2 + \gamma\tau^3, \tag{7}$$

where $x(t)$ is antenna position at time t, x_0 is current antenna position and τ is time difference between t and t_0 which is current time. To find the coefficients α, β, and γ, a system of linear equations needs to be solved:

$$x(\Delta\tau) = x_1,\ x_1' = \alpha + 2\beta\Delta\tau + 3\gamma\Delta\tau^2,\ x_0' = \alpha, \tag{8}$$

where x_1 is coordinates of an object, x'_1 is velocity of this object, x'_0 is current velocity of the antenna and $\Delta\tau$ is time difference between current time (t_0) and time needed to reach the source trajectory (t_1).

All of the variables necessary to find α, β, and γ are known, except for time t_1 which is found in iterative way moving point x_1 until it is possible to create a trajectory, which leads the antenna without exceeding its maximum possible velocity.

A simple reach ability test is performed when a potential trajectory is calculated in order to check whether the antenna can make this trajectory without exceeding its maximum acceleration and velocity.

5. RESULTS AND DISCUSSION

To check the polynomial-based tracking algorithm, test observations have been performed. Several objects have been tracked. Logged observational data have been used as input to get model results. We have analysed five test cases that simulate real EVN sessions. In addition to the experiments with real antenna, the model antenna described in Section 3 has been used with even more EVN session motion schedules. For the same schedules the model appears to be sufficiently good to replace a real antenna. An example of a typical EVN session schedule with results of experiment and simulations is shown in Fig. 4(a).

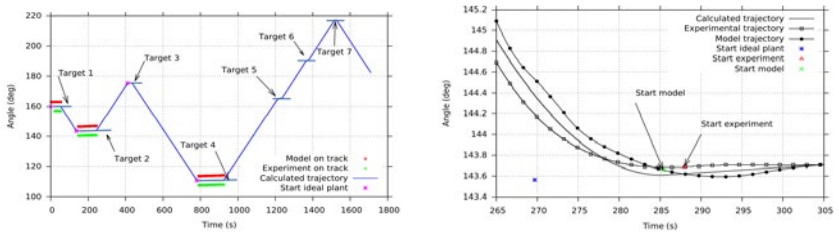

(a) (b)

Fig. 4. Example of EVN session with seven observational targets (a). Observational object trajectories are shown with horizontal lines. Comparison of an antenna trajectory during tracking using an ideal plant, experimental, and model results (b).

Time and position, when the ideal plant is on the source trajectory is marked with a star in Fig. 4(a). Time when a model and an experiment are on observational object trajectory is marked with a square (above theoretical trajectory) and circle (below theoretical trajectory), respectively. Both the modelled and experimental trajectories have not fulfilled conditions to observe Target 3; however, theoretically it should have been observed. There are three cases (Target 5, Target 6, and Target 7), where calculated observational time of the object is less than 20 seconds; therefore, it is assumed that objects have not been observed.

The effectiveness of the tracking algorithm has been calculated as the ratio of tracking time of controlled antenna to the tracking time of an "ideal" antenna. In both

cases antenna must be on trajectory of the object for at least 20 seconds before counting starts (for initial data collection needed for cross-correlation). For an "ideal" case we assume that the antenna (plant) reaches trajectory of the object trajectory (marked with a star in Fig. 4(b)) at a maximum hardware velocity and follows an absolute and stable tracking after.

Results of five test cases are summarised in Table 1. Results show that on average time (T0) spent for antenna movement between observational objects takes from 64 % (model and experiment) till 66 % (ideal plant) of all the time of a particular session. An "ideal" case has no pointing and settling time (T1); therefore, T0 is larger than in the model and experiment. Time (T1) is from 3 % till 9 % depending on the case (for model and experiment). On average, the efficiency of the controller is lower by 12 % when compared to an ideal plant (unreachable condition) while the experiment efficiency is lower by 14 %. In all cases when an ideal plant has not observed a target, it happened due to observational 20 second start-up limit discussed above. Model and experiment have not observed sources also due to large settling time (oscillations of the antenna).

Table1

Division of Normalized Time Regions of Different Observation Sessions

Cases	Type		T0	T1	T2	Targets (observed/ total)
Case 1	PID	Ideal	0.678	-	0.322	8/10
		Model	0.645	0.077	0.278	6/10
		Exp		0.090	0.265	6/10
Case 2	PID	Ideal	0.529	-	0.471	6/8
		Model	0.548	0.029	0.433	4/8
		Exp	0.567	0.057	0.377	3/8
Case 3	PID+AA	Ideal	0.607	-	0.393	6/8
		Model	0.569	0.061	0.370	6/8
		Exp		0.079	0.352	6/8
Case 4	PID+AA	Ideal	0.678	-	0.322	8/10
		Model	0.632	0.080	0.288	7/10
		Exp	0.619	0.072	0.309	8/10
Case 5	PID+AA	Ideal	0.809	-	0.191	4/7
		Model	0.817	0.030	0.153	3/7
		Exp		0.030	0.153	3/7

Both the experimental and modelling results show that an improved algorithm (PID+AA) that uses the 3rd-order polynomial and considers current antenna velocity when calculating a trajectory allows reaching a target sooner and consumes less time for pointing and settling than previously used methods (PID). As can be seen in examples provided in Table 2, the average value of time region T1 for a single target using only a PID controller is 60.95 s whereas using PID with an additional algorithm is 31.61 s.

Table 2

Average Value (in Seconds) of Correction Region T1 (Pointing and Settling Time) for Single Observational Target

Cases	Type	Average time of T1 for a single object (s)
Case 1	PID	57.73
Case 2	PID	64.17
Case 3	PID+AA	29.49
Case 4	PID+AA	39.51
Case 5	PID+AA	25.82

6. CONCLUSIONS

Smooth trajectory generation approach has been developed and applied to the existing PID controller of antenna. We have developed a dynamical model of servo system to be able to analyse more observation sessions with no need of use of expensive time of real antenna and to perform case studies by comparing various control algorithms. Despite mechanical robustness of the radio telescope RT-32, our telescope model results fit well with the experimental values.

Third-order polynomial-based trajectory generation algorithm has been worked out and tested. Test observations with RT-32 have been done to check the improved approach. Experimental and model results (as well as theoretical considerations) show that a 3rd-order polynomial trajectory generator ensures fewer oscillations of the antenna when moving from one object to another than relying only on switching on or off a basic PID control algorithm.

ACKNOWLEDGEMENTS

Research is presented as part of Project No. L-KC-11-0006, funded by the European Regional Development Fund.

REFERENCES

1. Gawronski, W., and Souccar, K. (2005). Control systems of the large millimeter telescope. *IEEE Antennas and Prop. Mag. 47* (4), 41–49.
2. Astrom, K.J, and Hagllund, T. (1995). *PID Controllers Theory, Design and Tuning*, 2nd ed. Instrument Society of America.
3. Ogata, K. (2002). *Modern Control Engineering,* 4th ed. New Jersey: Prentice Hall.
4. Astrom, K. J. and Murray, R. M. (2010). *Feedback Systems. An Introduction for Scientists and Engineers,* 2nd ed. Princeton, Oxford: Princeton University Press.
5. Peng, Y., Vrancic, D., and Hanus, R. (1996). Anti-windup, bumpless, and conditioned transfer techniques for PID controllers. *IEEE Control Systems*, *16* (4), 48–57.
6. Kanamori, M. (2013). Anti-windup adaptive tracking control for Euler-Lagrange systems with actuator saturation. In *3rd Int. Conf. on Instr. Control and Automation*, 28–30 August 2013 (pp. 216–221).
7. Mandarapu, S., Lolla, S., and Kumar, M.V.S. (2013). Digital PI controller using anti-wind-up mechanism for a speed controlled electric drive system. *Int. J. of Innovative Tech. and Exploring Eng. 3* (1), 239–242.

8. Hu, K., et al. (2013). Simulation and analysis of LQG controller in antenna control system. In *IEEE 4th Int. Conf. on Electronics Information and Emergency Communication*, 15–17 November 2013 (pp. 268–273).
9. Gawronski, W. (2001). Antenna control systems: from PI to H∞. *IEEE Antennas and Prop. Mag. 43* (1), 52–60.
10. Gawronski, W. (2002). *A Command Preprocessor for Antenna Motion without Overshoots*. Interplanetary Network Progress Report. Pasadena, California: Jet Propulsion Laboratory.
11. Smith, D.R., and Souccar K. (2008). A polynomial-based trajectory generator for improved telescope control. In *Proc. SPIE 7019, Advanced Software and Control for Astronomy II*.
12. Rivetta, C., Briegel, C. and Czarapata, P. (2000). Motion control design of the SDSS 2.5 mts telescope. In *Proc. SPIE 4004, Int. Soc. Opt. Eng. 2000*(pp. 212–222).

GLUDAS SEKOŠANAS TRJEKTORIJAS IZVEIDE LIELĀM ANTENĀM

S. Upnere, N. Jēkabsons, U. Locāns

K o p s a v i l k u m s

Antenu un teleskopu kontroles sistēmai jānodrošina precīza uzvadīšana un sekošana novērojamam objektam.

Vadīšanas precizitāti ietekmē gan antenas tehniskie parametri (maksimālais pārvietošanās ātrums un paātrinājums, motoru griezes moments utml.), gan izmantotie kontroles algoritmi.

Šajā publikācijā ir aprakstīts pilnveidots kontroles algoritms, kas uzlabo mehāniski robusta, liela radioteleskopa sekošanu vairākiem novērojamiem objektiem pēc kārtas. Lai samazinātu PID kontroliera izraisītas antenas oscilācijas laikā, kad tā sasniedz mērķa trajektoriju, pārvietojoties no viena pētāmā objekta uz citu, tiek izmantots papildus trešās kārtas polinoms, kas ļauj izveidot gludu uziešanu uz mērķa trajektorijas.

Radioteleskopa RT-32 dinamiskais modelis ir izveidots, lai analizētu novērojumu sesijas pirms to uzsākšanas, kā arī, lai novērtētu kontroles algoritmu efektivitāti. Uzlabotais kontroles algoritms tika pārbaudīts gan izmantojot reālus EVN novērojumu sesijas grafikus ar RT-32, gan radioteleskopa dinamisko modeli. Abos gadījumos rezultāti apstiprina, ka 3. kārtas polinoma izmantošana trajektorijas izveidē samazina antenas oscilācijas sasniedzot mērķa trajektoriju.

27.08.2015.

LATVIAN JOURNAL OF PHYSICS AND TECHNICAL SCIENCES
2016, N 1

DOI: 10.1515/lpts-2016-0004

RESEARCHING AND DESIGNING PHOTOVOLTAIC MICROSYSTEMS

D. Hilse[1], J. Kapała[1], K. Sztymelski[2], N. Zeltins[3], J. Ekmanis[3]

[1]University of Bielsko-Biala, Faculty of Materials, Civil and Environmental Engineering, Institute of Environmental Protection and Engineering
ul. Willowa 2, 43-309 Bielsko-Biala, POLAND
Email: biuro@hilkap.eu
[2]Silesian University of Technology, Faculty of Electrical Engineering, Institute of Industrial Electrical Engineering and Computer Science
ul. Akademicka 10, 44–100 Gliwice, POLAND
[3]Latvian Member Committee of WEC
Akademijas laukums 1-1, LV-1050, Riga, LATVIA

Research on the photovoltaic module efficiency in the south of Poland was conducted in 2009 in Stryszawa and afterwards in 2012 in Zabrze and Stryszawa. The research involved taking measurements of electric energy produced by systems of various power and technical solutions. The efficiency of PV modules was compared to the intensity of solar radiation in the locations under consideration and, thus, the efficiency of converting solar energy into electricity was determined. The research results facilitated designing and mounting of forty PV microsystems in Zabrze in 2014 (power from 2000 Wp to 3000 Wp). To the satisfaction of their users, they operate without failure.

Keywords**:** *converting solar energy into electricity, photovoltaic, PV modules and systems, solar radiation.*

1. INTRODUCTION

Poland does not belong to countries characterised by the highest potential of solar energy, which is 850 ÷ 1300 kWh/m$^2_*$year, whereas in equatorial countries, South America and Africa it exceeds 2200 kWh/m$^2_*$year [1]. Nevertheless, the possessed potential is sufficient to cover 1/3 of the need of energy in Poland [2].

In practice, making use of the possessed potential of solar energy should not pose major technical problems, in case photovoltaic cells in the form of photovoltaic modules are applied. They are indispensable for designing and mounting of microsystems producing low-voltage current, which is used:

- directly, e.g. to illuminate squares, streets, real estates, or places which are difficult to connect to mains power supply;
- after it is converted into 230 V current.

In the second case, the installation can be off-grid or on grid.

Off-grid systems are used as independent (in case of objects without the external power grid) or as emergency (when frequent power outages occur). It comprises: photovoltaic modules, batteries, charge regulators, transducers.

On-grid systems enable "mixing" electric energy produced by photovoltaic modules and electricity provided by the external power grid. They do not require using batteries, due to the fact that the excess of produced energy can be resold to the distributor.

Designing and constructing photovoltaic systems, off-grid microsystems in particular, should be based on precise determination of solar radiation at certain times in a certain area, with simultaneous evaluation of installed photovoltaic module efficiency.

In particular, it concerns mountainous areas, where the intensity of solar radiation changes significantly even during one day, depending on the topography [3].

The paper presents the results of the research on the efficiency of several photovoltaic systems in two locations in Poland:

- Zabrze (city at an altitude of 239 meters, geographical coordinates – 50°19'29" N, 18°47'8" E);
- Stryszawa (village at an altitude of 591 meters, geographical coordinates – 49°40'54" N, 19°29'0" E).

They were used for designing and mounting of numerous PV microsystems (on-grid), inter alia in the territory of Zabrze.

2. EXPERIMENTAL SYSTEMS, METHODS AND RESEARCH RESULTS

The first series of research (in 2009) consisted in mounting three PV systems in the experimental station in Stryszawa, which are the following [3]:

1. a system comprising three photovoltaic modules with power of 3 x 190 Wp = 570 Wp and total surface of 5.2 m^2; modules were mounted on a rotating frame (tracking the movement of the Sun), in an open space;
2. a system comprising two photovoltaic modules with power of 2 x 180 Wp = 360 Wp and total surface of 3.4 m^2; modules were mounted on a stationary frame, in an open space;
3. a system comprising one photovoltaic module with power of 200 Wp and total surface of 1-9 m^2; the module was mounted on the southern wall of a residential building.

Experimental systems contain the following elements:

- photovoltaic modules;
- battery charge regulators;
- batteries (accumulating direct current 12 or 24 V);
- transducers – inverters, changing direct current into alternating current 230 V;
- meters of energy units produced and transmitted to consumption.

The experimental station performed a function of an off-grid system, in which

the current was used directly by the producer, and the produced excess was used by the engine working uselessly at an idle speed.

The third system is able to operate on direct current (24 V), with illumination and supplying buffers of central heating as the aims of generated electricity.

The amount of energy generated by the systems described above was measured using typical meters, which were read at the end of every month in 2009. The obtained results were compared to the values of intensity of solar radiation in Żywiec (the distance from the experimental station is less than 20 km), taken from the Silesian Air Monitoring database [5].

The results of research conducted in 2009 are summarised in Tables 1–3 [3].

Table 1

The Efficiency of FV Modules at the Experimental Station in Stryszawa in 2009

Month	**Electricity production, kWh/m²**		
	System 1	System 2	System 3
I	24.4	12.6	5.9
II	27.6	14.3	6.8
III	49.9	26.2	12.4
IV	114.4	56.1	28.3
V	102.4	48.6	25.1
VI	82.2	40.5	20.7
VII	99.3	45.6	23.4
VIII	111.3	51.0	25.7
IX	80.6	39.4	19.8
X	41.6	20.4	9.9
XI	37,4	19.7	9.3
XII	12,5	6.1	2.8
2009	783,6	380.5	190.1

Table 2

The Efficiency of FV Modules in Stryszawa Compared to the Intensity of Solar Radiation

Month	**Intensity of solar radiation, kWh/ m² * month**	**Electricity production, kWh/ m² * month**		
		System 1	System 2	System 3
I	20.42	4.7	3.7	3.1
II	20.40	5.3	4.2	3.6
III	42.96	9.6	7.7	6.5
IV	133.15	22.0	16.5	14.9
V	124.80	19.7	14.3	13.2
VI	102.24	15.8	11.9	10.9
VII	151.27	19.1	13.4	12.3
VIII	126.19	21.4	15.0	13.5
IX	86.76	15.5	11.6	10.4
X	38.02	8.0	6.0	5.2
XI	28.77	7.2	5.8	4.9
XII	15.10	2.4	1.8	1.5
2009	890.08	153.4	111.9	100.0

Table 3

The Efficiency of Converting Solar Energy into Electricity at the Experimental Station in Stryszawa

Month	Efficiency of energy conversion, %			Average air temperature, C° (over the period 1971–2000)
	System 1	System 2	System 3	
I	23.02	18.12	15.18	- 1.7
II	26.00	20.59	17.65	- 2.3
III	22.35	17.92	15.13	4.9
IV	16.52	12.39	11.19	8.0
V	15.80	11.46	10.58	12.4
VI	15.45	11.64	10.66	16.2
VII	12.65	8.86	8.13	19.2
VIII	16.96	11.89	10.70	17.1
IX	17.87	13.37	12.00	15.1
X	21.04	15.78	13.68	8.9
XI	25.03	20.16	17.03	4.4
XII	15.89	11.92	9.93	0.1
2009	17.23	12.57	11.23	

From the conducted research, it can be inferred that rotating modules have the highest efficiency, making use of the sun's rays during the whole cycle.

In mountain conditions of Beskid Żywiecki, in Stryszawa to be more specific, they can produce more than 150 kWh/m^2 * year. The efficiency of stationary modules mounted in open spaces (or on roofs of buildings) is approximately 25 % lower. The same modules mounted on a façade of a building have 35 % lower efficiency.

Calculated efficiency of converting solar energy into electricity is provided in Table 3. Among others, this factor depends on the temperature of surrounding air. In this case, the highest efficiency, exceeding 17 % annually, was noted in case of rotating modules, reaching the highest values (up to 26 %) in the winter season.

The above data indicate that as far as FV systems are concerned, the conditions in Stryszawa village are moderately favourable to produce electricity.

The ***second series of research (in 2012)*** on the PV system was conducted in Stryszawa as well as in Zabrze.

In Stryszawa, the measurements of the rotating system, already discussed above, were continued. In Zabrze, on the other hand, a stationary system was mounted on a flat roof of a residential building, equipped with four modules with power of 4 x 250 Wp = 1000 Wp and total surface of 6.4 m^2. Both the above-mentioned systems are off-grid type.

The way of conducting measurements was identical to the first series.

During the research, the efficiency of PV systems in relation to the intensity of solar radiation was determined. The measurement results are summarised in Table 4 (rotating module in Stryszawa) and in Table 5 (stationary module in Zabrze). In this part, for the purpose of comparison, PVGIS European Union, 2001–2012 was used [6].

The results of measurements and conclusions drawn from the second series of the research confirm previous findings, namely:

a) taking into consideration the conditions in southern Poland, it is sensible to use solar energy in order to produce electricity with the aid of photovoltaic microsystems;
b) rotating systems are more efficient than stationary photovoltaic systems.

Table 4

The Efficiency of a Rotating Module in Stryszawa in Relation to the Intensity of Solar Radiation in 2012

Month	Intensity of solar radiation, kWh/ m^2 * month	Electricity production, kWh/ m^2 * month
I	34.2	5.45
II	46.2	7.35
III	99.0	15.17
IV	135.0	20.40
V	141.0	21.40
VI	135.0	20.40
VII	150.0	22.30
VIII	145.0	21.93
IX	105.0	16.25
X	77.3	12.20
XI	42.0	6.80
XII	30.2	4.42
2012	1140.0	174.0

Table 5

The Efficiency of a Stationary Module in Zabrze in Relation to the Intensity of Solar Radiation in 2012

Month	Intensity of solar radiation, kWh/ m^2 * month	Electricity production, kWh/ m^2 * month
I	33.1	4.42
II	50.9	6,63
III	110.0	13.90
IV	148.0	17.97
V	161.0	19.06
VI	158.0	18.28
VII	165.0	19.06
VIII	158.0	18.28
IX	117.0	14.11
X	84.5	10.47
XI	42.5	5.49
XII	31.0	4.08
2012	1260.0	151.72

3. DESIGNING AND CONSTRUCTING PHOTOVOLTAIC MICROSYSTEMS IN ZABRZE

The awareness of the issues discussed above and research results facilitated designing and constructing 40 photovoltaic microsystems in Zabrze in 2014, each with power from 2000 Wp to 3000 Wp. The total cost of one system (design, materials and components, mounting, commissioning, handling formal and legal matters, and others) was from 12500 PLN to 15000 PLN (where 1 € = approximately 4.1 PLN). The microsystems were mounted on private residential buildings, with the subsidy of the Municipal Office of Zabrze – up to 12000 PLN of financial support for each system [4].

At the request of the majority of investors, on-grid type systems were mounted, which resulted in an additional reduction of investment costs, due to the elimination of expensive and problematic batteries.

An example of an implemented investment is a microsystem consisting of 8 PV panels, polycrystalline, with power of 8 x 250 Wp = 2000 Wp. They are connected in a string. One-phase STECA Coolcept 1800 inverter was used as an on-grid inverter, with maximum power of 1.84 kW. It enables the over-dimensioning of DC system up to 30 %, which enhances the operation of MPPT system and higher efficiency of the system in case of a partly clouded sky and an unbeneficial position of the sun.

PV panels were mounted on a flat roof, in one row, at a fixed angle of 32° and approximately 200° SSW.

PV systems are connected into the public grid by energy supplies (in this case TAURON Polska Energia). Electricity gross meters as well as bidirectional meters are provided and installed by TAURON, at the expense of the company. All the activities, including preparing an appropriate location necessary for placing meters, with protective seals before and behind the meter, designing and drawing diagrams of installations, are performed by a person with proper qualifications.

In order to minimise losses, as for DC, connections were made using a dedicated silver plated wire with cross section of 6 mm^2, containing a single conductor, with insulation characterised by higher resistance against UV radiation.

All the connections were made using dedicated, tight MC4 connectors. The electrical wiring was installed in an electrical conduit, so that different elements of the DC system could be gathered in one place. Furthermore, placing wires in electrical conduits prevents arising unbeneficial static magnetic fields. As for AC, all the connections were made using YLgYżo cable (3x2.5 mm^2).

The heart of the on-grid type PV system is an on-grid inverter. This device cannot be off-grid (disconnected from the grid). The choice of the inverter was not accidental. Apart from all possible DC and AC protectors, this inverter is equipped with a built-in web server, the function of registering the amount of generated electricity: daily, monthly or annually, every 30 days, months or years. It also has a built-in network interface card and RS485 interface, allowing reading and storing data. Its expanded menu enables to exert influence on the frequency, PF coefficient and reactive power generation. The output active power can be reduced manually.

The above-mentioned options make it possible to perform a thorough analysis of a PV system.

Electricity meters installed by TAURON, the so-called "intelligent meters", are provided with a transmission service. On a website, to which the owner of the system has an access, it is possible to monitor the amount of used, generated and produced gross energy with accuracy of 1 h. The data can be downloaded as an excel file.

An example of visual presentation of the amount of generated and used energy, for a PV microsystem with power of 2 kWp – on-grid, is shown in Fig. 1.

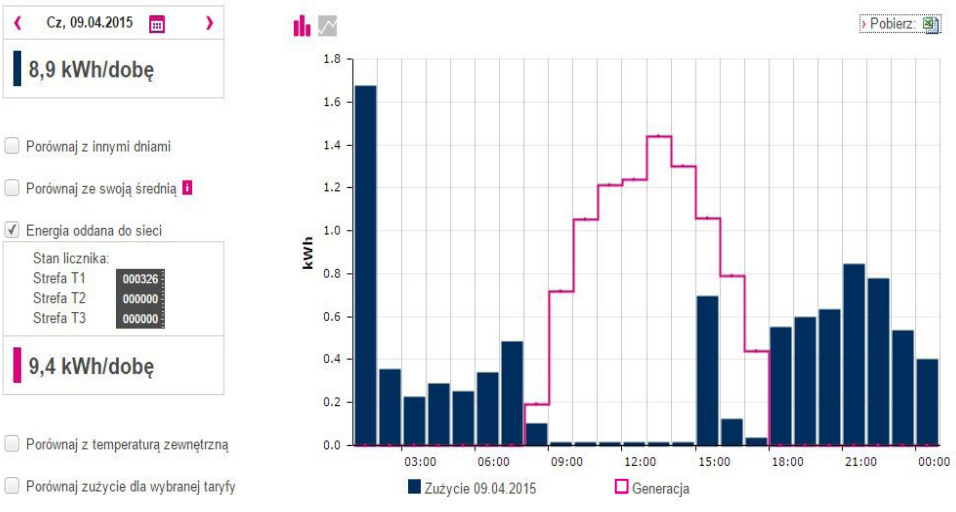

Fig.1. Visual presentation of energy use and generation.

4. CONCLUSIONS

The conducted research and analyses indicate that as far as electricity production using PV systems is concerned, conditions in southern Poland are moderately favourable. In this region, average annual electricity production in this kind of systems is 110÷175 kWh/m^2, when the intensity of solar radiation is 890÷1260 kWh/m^2. PV systems with the highest efficiency are the ones equipped with modules on rotating frames, whereas systems on stationary frames prove to have 20÷25% lower efficiency. The highest monthly efficiency of converting solar energy into electricity can be noted in winter months (XII, I, II).

In 2014, based on the research results obtained so far, 40 micro on-grid type photovoltaic systems with power from 2000 Wp to 3000 Wp were designed and mounted in Zabrze. One of them has been thoroughly discussed above. The results of their operation, after almost a year of operating, are very encouraging. This has been followed by a rapidly increased interest in mounting further PV microsystems across the country.

REFERENCES

4. Martyn, D. (1995). *Klimaty kuli ziemskiej*. Wydawnictwo Naukowe PWN, Warszawa.
5. Hilse, D. and Kapała J. (2011). Fotowoltaika-elektryfikacja bezdrutowa. *Fotowoltaika* 1, 16–17.
6. Hilse, D. and Kapała J. (2013). Badania wydajności modułów fotowoltaicznych. *Inżynieria Ekologiczna* (Ecological Engineering) 33, 41–48.
7. Hilse, D. and Kapała J. (2014). Lampy oświetleniowe hybrydowe. *Fotowoltaika* 4, 10–11.
8. Śląski Monitoring Powietrza. Available at /http://stacje.katowice.pios.gov.pl/iseo/
9. PVGIS Europäische Union, 2001–2012. Available at http://re.jrc.ec.europa.eu/pvgis/apps4/pvest.php?lang=de&map=europe

FOTOELEMENTU MIKROSISTĒMU PĒTĪJUMI UN PROJEKTĒŠANA

D. Hilse, J. Kapała, K. Sztymelski, N. Zeltiņš. J. Ekmanis

K o p s a v i l k u m s

Saules moduļu efektivitātes pētījumi tika veikti Polijas dienvidos 2009. gadā Stryszawā un 2012. gadā Zabrzē un Stryszawā. Pētījuma ietvaros tika veikti sistēmu saražotās elektroenerģijas mērījumi dažādos režīmos un pie dažādiem tehniskajiem risinājumiem. PV moduļu efektivitāte tika salīdzināta pie dažādas saules starojuma intensitātes, dažādās vietās un dažāda elektroenerģijas pieprasījuma. Pētījuma rezultāti veicināja četrdesmit PV mikrosistēmu, ar jaudu no 2000 līdz 3000 Wp, projektēšanu un montāžu Zabržē 2014. gadā. Šīs sistēmas apmierināja to lietotājus, jo tās darbojas bez atteices.

29.07.2015.

LATVIAN JOURNAL OF PHYSICS AND TECHNICAL SCIENCES
2016, N 1
DOI: 10.1515/lpts-2016-0005

THE ISSUE OF CALCULATING THE FINAL TEMPERATURE OF THE PRODUCTS OF RAPID EXOTHERMIC CHEMICAL REACTIONS WITH SIGNIFICANT ENERGY RELEASE IN A CLOSED VOLUME

V. Lazarev, D. Geidmanis
Institute of Physics, University of Latvia,
32 Miera Str., Salaspils, LV-2169, LATVIA
E-mail: fizinst@sal.lv

The theoretical problem solved in this article is the calculation of thermodynamic parameters such as final temperature, distribution of the liquid and dry saturated vapour phases of the substance that are considered to be in thermodynamic equilibrium, and pressure of the system of several reaction products after adding to the system a certain amount of heat or the thermal effect released during rapid exothermic reaction in a closed volume that occurs so fast that it can be considered to be adiabatic, and when the volume of liquid reagents is several orders of magnitude less than the volume of the reactor. The general multi-substance problem is reduced to a theoretical problem for one substance of calculation thermodynamic parameters of system after adding a certain amount of heat that gives theoretically rigorous isochoric calculation. In this article, we substantiate our view that isochoric pass of calculation is more robust compared to seemingly more natural isobaric pass of calculation, if the later involves quite not trivial calculation of the adiabatic compression of a two-phase system (liquid – **dry** saturated vapour) that can pass itself into another kind of state (liquid – **wet** saturated vapour), which requires, apparently, more complex descriptions compared with isochoric calculation because the specific heat capacity of wet saturated vapour can be negative.

The solved theoretical problem relates to a practical problem that has been a driver for our research as part of a design of the reactor of the titanium reduction from magnesium and titanium tetrachloride supplied into atmosphere of the reactor at high temperatures when both reagents are in gaseous state. The reaction is known to be exothermic with a high thermal effect, and estimate of the final temperature and pressure of the products of reaction, for instance, designing the reactor allows eliminating the possibility of the reaction products to penetrate backwards into supply tracts of the reagents. Using a rigid theoretical approach and heuristics of thermodynamic parameters of reaction products available in the literature, we have presented a graphical dependence of final temperature, pressure ratio of the liquid and vapour state of titanium after the reaction on the initial temperature of the reactor and magnesium in the range of 1200–1800 °K while titanium tetrachloride is injected into reactor at its critical temperature.

Keywords: *final temperature of the reaction products, isochoric calculation, rapid exothermic chemical reaction*

1. INTRODUCTION

Thermal effect ΔH_{298} of exothermic chemical reactions [1] taking place in hermetically closed reactor volumes may be so large that the reaction products are in the gaseous state at very high pressures and temperatures. In such cases and especially when the initial temperature of the reactants is high, one of the important problems during designing of chemical reactors is estimating thermodynamic characteristics of the reaction products in the final state of the reaction process. If the reaction proceeds rapidly enough then the adiabatic condition can be applied to the theoretical calculation as a good approximation of the thermodynamic characteristics of the process, and they frequently are close enough to the maximum temperatures of the reaction observed experimentally.

In general, to determine the theoretical temperature of the reaction the heat balance of the process is made [2] as follows: the value of the total amount of heat - ΔH_{298} together with the sum of the enthalpies of the reactants is obtained for a temperature at which they enter the reaction, then after the reaction the product is heated by this heat from 298°K to the desired temperature considering also the heat of polymorphic transformations, melting and evaporation of reaction products, etc., the process equation is developed and then it is solved with respect to the reaction temperature.

It is not difficult to calculate the heating process and the final temperature of the reaction products assuming that the heating process is isobaric. This corresponds to the situation when the volume of the reactor must be increased in the course of the reaction to maintain the pressure at the baseline level. The volume during the theoretical isobaric calculation has been increased. It is necessary to establish a further adiabatic compression of the reaction products to the original volume. However, during this theoretical compression process of the reaction products, generally speaking, various phase transitions must be passed, including compression of dry saturated vapour and then compression of wet saturated vapour, which is a two-phase system where dry saturated vapour coexists in thermodynamic equilibrium with the liquid and at further compression condenses into a liquid phase, and so on. The complexity of the last part of calculation path described above depreciates relative ease of the part of isobaric calculation. Therefore, generally speaking, if possible such a pass of calculation should be avoided unless there is a substantial reasoning to do otherwise, and we regard that direct isochoric calculation may be a safer and easier approach, especially if the reaction is fast and the adiabatic condition can be regarded as a good approximation. It should be noted that the heating process in the solid phase, including melting, complies with the isochoric condition and can be taken from the isobaric calculation. It should also be noted that the heating of the reaction products in the form of wet vapour – a two-phase system, where dry saturated vapour coexists in thermodynamic equilibrium with the liquid phase in a constant closed volume – is the most problematic part of the calculation. The peculiarity of the processes in two-phase systems (isochoric heating, quantitative ratio of the phases at the end of the reaction, adiabatic compression and others) is related ultimately to the fact that the specific heat capacity of dry saturated vapour of any substance, in general, is negative [4], [5]. As the distance from the critical point increases, specific heat remains negative but its absolute value decreases, then it becomes zero and during further

increase becomes positive. In these conditions, negative specific heat means that heating (rising of the temperature) of saturated vapour causes it to release a certain amount of heat. The isochoric evaporation of liquid is a kind of process that in our opinion should be best described in a general way on the basis of the theory developed in [3]. It should be noted that the adiabatic compression of a two-phase system (liquid – **dry** saturated vapour) can pass itself into another kind of state (liquid – **wet** saturated vapour) [3], which requires, apparently, more complex descriptions compared with isochoric heating.

Next, we present a thermodynamic calculation of the adiabatic heating of a two-phase system consisting of dry saturated vapour coexisting in thermodynamic equilibrium with the liquid phase, enclosed in a volume of constant size, when a certain amount of heat is added to the system.

The theoretical calculation will be further applied in order to get assessment of the final temperature of the reaction $TiCl_4+2Mg \rightarrow 2MgCl_2+Ti$ in a closed volume of a reactor of constant certain size and temperature that happens there, assuming that both ingredients are in a gas-vapour phase of the same temperature as the body of the reactor.

2. PROBLEM STATEMENT

Two phases – liquid and its dry saturated vapour – of a homogeneous substance are situated in a closed volume of constant size in a thermodynamic equilibrium at temperature T_1, where m' is the mass of the liquid, m'' is the mass of the dry saturated vapour, and $m'+ m''=m=const$.

We consider that the two-phase system is isolated, and a certain amount of heat Q is added to it so that the system performs a transition from one thermodynamic equilibrium state of phases at the temperature T_1 to a new thermodynamic equilibrium state of phases at the temperature T_2 to be found. Our task is to calculate T_2 as well as a quantity ratio of the masses of both phases of the system at the end of the process. Considering our reaction proceeds rapidly, we neglect interaction with the walls, so the process is considered to be adiabatic. Temperature range is limited from below by melting temperature T_m of liquid, and from the top by temperature T_{ev} in which all the liquid mass m' in volume V would evaporate and all the substance would become dry saturated vapour. In order to comply with the above condition, value of Q should not exceed the one that is necessary to evaporate the entire mass m' of the liquid.

It is important to note that the thermodynamic equilibrium phase transition at volume $V = const$ means that the isochoric process applies to the system as a whole so that the liquid phase process is on the left of the boundary curve, while the saturated vapour process is on the curve at the right boundary, i.e. the vapour at all times remains only dry saturated vapour [1].

3. NOTATIONS

T – the absolute temperature.

$P_v\ (T)$ – the pressure of dry saturated vapour at temperature T (i.e., all the vapour is under thermodynamic equilibrium with the liquid; it is not superheated vapour, and

no saturated liquid or wetness is present in the atmosphere, and therefore all the liquid if any exists only in the bottom of volume of the considered system).

Q – the quantity of heat.

V; v – the volume and specific volume of the system.

U; u – the internal energy and specific internal energy of the system.

I; i – the enthalpy and specific enthalpy of the system.

$r(T)$ – the specific heat of vaporisation

Once primed quantities refer to the liquid phase, and doubly primed quantities belong to the vapour phase.

c'; c'' – the specific heat capacity (liquid and gas) phases of the system.

V'; V''; v'; v'' – the volume and specific volume of the substance in the system in respective phases at given temperature T of the system.

U'; U''; u'; u'' – the internal energy of the substance of the system in the respective phases and the specific internal energy phases of the system at given temperature T of the system.

I';I''; i'; i'' – the enthalpy and specific enthalpy of the system in the respective phases at given temperature T of the system.

Given the above notation, we can write:

$$V = m \cdot v = V' + V'' = m \cdot (v' + v'')$$
$$U = m \cdot u = U' + U'' = m \cdot (u' + u'')$$
$$I = m \cdot i = I' + I'' = m \cdot (i' + i'') .$$

4. THEORY

It should be noted that all the components of the equation of thermodynamic state of the system are functions of temperature T of the system, which has both liquid and vapour that are in the thermodynamic equilibrium. As described in the previous section, we avoid dealing with the so-called wet vapour and, therefore, consider that the entire mass of the system consists either of liquid or dry saturated vapour. Therefore, we consider that at any temperature T of the system the equation holds: $m=m'+m''$.

Since the process is isochoric, all the heat added to the system increases the internal energy of the system:

$$dQ = dU = dU' + dU'' \tag{1}$$

Adding to the system some heat dQ, part of the mass of the liquid phase converts into vapour, and the distribution of energy is obtained as follows:

$$dU' = d(m' \cdot u') = m' \cdot du' + u' \cdot dm' \tag{2}$$

$$dU'' = d(m'' \cdot u'') = m'' \cdot du'' + u'' \cdot dm'' \tag{3}$$

Here, we assume that each next state after adding additional heat dQ is also in thermodynamic equilibrium and contains either dry vapour or liquid, and the atmosphere in the volume of the system does not contain wet vapour. Therefore, the equation holds *m'=m-m"* and *dm'= –dm"*.

Since $i=u+P\cdot v$ and process is isochoric $di=du+P\cdot dv+v\cdot dP$, $di=du+v\cdot dP$. Given that the change in temperature of the system is possible only by changing the mass distribution of the system between the liquid and vapour phase, with increasing temperature some part of the liquid will evaporate and conversely. Therefore, when calculating the specific enthalpy of the system it is required to take into account the specific heat of evaporation *r (T)* required for the phase transition. We have: $i''=i'+r$, $u'= i' - P_v\cdot v'$ and $u''=i''-P_v\cdot v''$.

$$u'' = (i' + r) - P_v \cdot v'' + (P_v \cdot v' - P_v \cdot v') = (i' - P_v \cdot v') + r + \\ + P_v \cdot (v' - v'') \text{ and we get:} \\ u'' = u' + r + P_v \cdot (v' - v'') \tag{4}$$

Thus, the overall relationship between the specific internal energy of system *u'* and *u"* is given by equations (6–54) and (6–61) from [3].

$$\int_{T_0}^{T} dU' = u'(T) - u'(T_0) = \int_{T_0}^{T} c' \cdot dt - \int_{T_0}^{T} P_v \cdot \frac{dv'}{dt} \cdot dt \tag{5}$$

$$c'(T) = c_p(T) - T \cdot \left(\frac{\partial v'}{\partial T}\right)_p \cdot \frac{dP_v}{dT} \tag{6}$$

where $c_p(T)$ – specific isobaric heat capacity of the liquid phase,
$u_0' = u'(T_0)$ – specific internal energy at certain temperature T_0.
Substituting (2) and (3), (4) (1) we obtain the following transformations:

$$dQ = dU = dU' + dU'' = m \cdot du' + d\{[r + P_v \cdot (v' - v'')] \cdot m''\} \tag{7}$$

Integrating (7) from temperature T_1 of the initial state to temperature T_2 of the final state of the system, we find heat Q that has been added to the system:

$$Q = U(T_2) - U(T_1) = m \cdot \int_{T_1}^{T_2} c' \cdot dt - m \cdot \int_{T_1}^{T_2} P_v \cdot \frac{dv'}{dt}\, dt + \\ + r_{liq}(T_2) \cdot m''(T_2) - r_{liq}(T_1) \cdot m''(T_1) + \\ + P_v(T_2) \cdot [v'(T_2) - v''(T_2)] \cdot m''(T_2) - \\ - P_v(T_1) \cdot [v'(T_1) - v''(T_1)] \cdot m''(T_1) \tag{8}$$

Equation (8) together with (6) gives the solution to the problem statement in a general form, and gives the equation of state of vapour to calculate $m''(T_1)$ and $m''(T_2)$, as well as gives formulas for the calculation of: $P_v = P_v(T)$ saturated vapour pressure;

$c_p = c_p(T)$ specific isobaric heat capacity of the liquid phase;

$r_{liq} = r_{liq}(T)$ specific heat of vaporisation of liquid

density of the liquid phase depending on temperature $\rho_{liq} = \rho_{liq}(T)$, and assessment of $\left(\frac{dv'}{dt}\right)_p$ and $\frac{dv'}{dt}$.

Taking into account

$$P_v(T_2) \cdot [v'(T_2) - v''(T_2)] \cdot m''(T_2) = - P_v(T_2) \cdot \left[V - V'(T_2) - \right. \\ \left. - \frac{m''(T_2)}{\rho_{liq}(T_2)}\right] \tag{9a}$$

$$\mathrm{P_v}(T_1) \cdot [v'(T_1) - v''(T_1)] \cdot m''(T_1) = - P_v(T_1) \cdot \left[\mathrm{V} - V'(T_1) - \right. \\ \left. - \frac{m''(T_1)}{\rho_{liq}(T_1)}\right] \tag{9b}$$

$$\left(\frac{\partial v'}{\partial t}\right)_p = \beta(T) \cdot v'(T) = \frac{\beta(T)}{\rho_{liq}(T)} \tag{9c}$$

where $\beta(T)$ is the coefficient of the volumetric thermal expansion, as well as integrating by parts the second integral in (5)

$$\int_{T_1}^{T_2} \mathrm{P_v} \cdot \frac{\mathrm{dv'}}{\mathrm{dt}}\,\mathrm{dt} = \frac{\mathrm{P_v(T_2)}}{\rho_{\mathrm{liq}}(\mathrm{T_2})} - \frac{\mathrm{P_v(T_1)}}{\rho_{\mathrm{liq}}(\mathrm{T_1})} - \int_{T_1}^{T_2} \mathrm{v'(t)} \cdot \frac{\mathrm{dP_v}}{\mathrm{dt}}\,\mathrm{dt} \tag{9d}$$

we obtain (8) in its final form:

$$Q = U(T_2) - U(T_1) = m\int_{T_1}^{T_2} c_p(t)\,dt + m \cdot \int_{T_1}^{T_2} v'(t) \cdot \left[1 - \beta(t) \cdot t\right] \cdot \frac{dP_v}{dt}\,dt - \\ - m \cdot \left[\frac{P_v(T_2)}{\rho_{liq}(T_2)} - \frac{P_v(T_1)}{\rho_{liq}(T_1)}\right] + r_{liq}(T_2) \cdot m''(T_2) - r_{liq}(T_1) \cdot m'(T_1) - \\ - P_v(T_2) \cdot \left[v - v'(T_2) - \frac{m''(T_2)}{\rho_{liq}(T_2)}\right] + P_v(T_1) \cdot \left[v - v'(T_1) - \frac{m''(T_1)}{\rho_{liq}(T_1)}\right] \tag{10}$$

5. CALCULATION OF THE AMOUNT OF HEAT Q FOR EVAPORATION OF LIQUID IN GIVEN VOLUME V AND TEMPERATURE T_{EV}

For a given mass of substance with molecular weight μ in the volume *V=const* there is a temperature, which we will call **the temperature of complete evaporation** and denote by T_{ev}, in which all the mass m in volume V will evaporate becoming dry saturated vapour. This temperature can be estimated from the system of van der Waals equation with constants a; b appropriate to the substance, and the formula for vapour pressure (P_v)

$$\text{where} \left[P + \left(\frac{m}{\mu}\right)^2 \cdot \frac{a}{V^2}\right] \cdot \left(V - \frac{m}{\mu} \cdot b\right) = \frac{m}{\mu} \cdot R \cdot T_{\mathrm{ev}} \text{ where } P = \mathrm{P}_v(T_{ev}) \tag{11}$$

solved with respect to temperature T_{ev}. However, more accurately T_{ev} can be

determined if we know the temperature dependence of the density of dry saturated vapour $\rho_v = \rho_v(T)$. Obviously, $m = V \cdot \rho_v(T_{ev})$. Sources [6]–[9] propose and use a formula, which compared to the experiment gives the mean square error in the range of 2 %–4 %:

$$\rho_v(T) = \frac{\frac{\mu P v(T)}{RT}}{Z_c + (1 - Z_c)\cdot(1-x)^y}, \; where\, Z_c = \frac{P_c \cdot v_c}{R \cdot R_c}, \; x = T_{red}^{0,7}, \; y = 0{,}33 \cdot T_{red}^{0,7}, \quad reduced\, temperaure\, T_{red} = \frac{T}{T_c} \tag{12}$$

where P_c[MPa]; V_c[cc/mole]; T_c[° K] are critical parameters, $\rho_v(T)$[g/cc]; R = 8.314 [J/(mol·K)], and μ [g/mol] is molecular weight.

Value Q is obtained from (8) or (10) considering that T_1 is the initial temperature of liquid, $T_2 = T_{ev}$, $V'(T_{ev}) = 0$, $m''(T_2) = m$. ($m'(T_1)$ can be evaluated from (11) at $T = T_1$, $m = m'$ and solving it with respect to m'. Temperature dependence $\rho_{liq}(T)$ should be taken from the literature, for example, [6], [10], [11] or to estimate approximately from [8], [9].

In the continuous methods of production of titanium [12], this occurs when calculating evaporation of magnesium and titanium tetrachloride. When evaluating Q to completely evaporate liquid, it is required to put $T_1 = T_m$. But most of all, as noted in the introduction, the importance of a theoretically rigorous calculation of Q is preferred to estimate the temperature and pressure of gases and vapours, and phase ratio of the products of exothermic reaction, which is developed in the course of the reaction at high initial temperatures of the reagents. In this regard, the following reaction is typical

$$TiCl_4 + 2Mg = 2MgCl_2 + Ti \tag{13}$$

and it occurs in the gas-vapour phase with a sufficiently high initial temperature of reagents, and with significantly high standard thermal effect $\Delta H_{298} = 62.5$ [kcal/(g·mol)].

Below are presented the final results of calculation of temperature of reaction (13), the partial pressures of the reaction products of magnesium chloride $MgCl_2$ and titanium Ti, as well as calculation of the ratio of liquid and vapour phases of titanium depending on the initial temperature of the isothermal body of rector, which is also the temperature of the reagent magnesium of the reaction. V = 30 litres is the volume of the reactor. Before the start of the reaction, this volume contains the amount of magnesium that evaporates completely creating dry saturated vapour of magnesium at the given initial temperature of the reactor. Then gaseous titanium tetrachloride $TiCl_4$ in a stoichiometric ratio with magnesium is injected into the reactor always at the same temperature of 638 °K, which is its critical temperature.

The reaction product of magnesium dichloride $MgCl_2$ will always be in the vapour or gaseous state, but titanium Ti will be in a two-phase thermodynamic equilibrium state of liquid and dry saturated vapour. Due to the very rapid reaction with extensive evolution of heat, the heat transfer to the reactor walls during reaction can be neglected and considered that it starts only upon completion of the reaction.

Therefore, the interaction with the walls of the reactor is not considered in the calculation process, and the reaction is considered to be adiabatic.

We have done also calculations for various volumes of the reactor. Our calculations show extremely weak dependence of the final reaction temperature on the reactor volume for the same initial temperature, and the corresponding amount of the reagent Mg as described above – the amount that creates dry saturated vapour of Mg without the liquid phase, and $TiCl_4$ in stoichiometric proportion. Hence, the partial pressure of $MgCl_2$ and the pressure of saturated vapour Ti will be almost the same, which is confirmed by calculation.

The range of initial temperatures of the body of reactor covered by the calculation is 1200 °K–1800 °K, with the step of 5 °K. Equation (10) obtained in the previous section binds the temperature and other thermodynamic parameters of one substance with adding of a certain amount of heat. However, in our case the products of our reaction (13) consist of two substances that share the same volume. It should be noted that total volume of the reaction products in liquid form is by three orders of magnitude smaller than the reactor, and therefore we can neglect it. On the other hand, considering reaction products in the vapour and gas state – they can normally co-exist and share the same volume so that the total pressure is a sum of the partial pressures of each substance. Therefore, calculation of the final temperature and other thermodynamic parameters for each substance using equation (10) can be done independently disregarding that they share the same volume, assuming that the volume of reactor is sufficiently big as in our case.

For each given increment of temperature, we can calculate independently for each substance the heat required for the said temperature increase, and can calculate the sum of the calculated heat. For the given standard thermal effect of the given exothermic chemical reaction, we can calculate the final temperature and other thermodynamic parameters of the products of reaction.

6. RESULTS

The results of calculations are presented in Figs. 1–3.

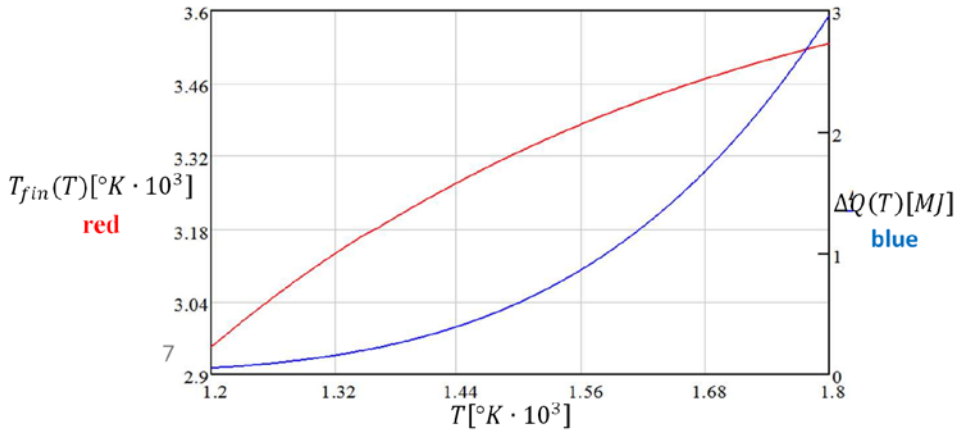

Fig. 1. Dependence of the final temperature and heat on the initial temperature of the reactor and magnesium, and injecting titanium tetrachloride at its critical temperature.

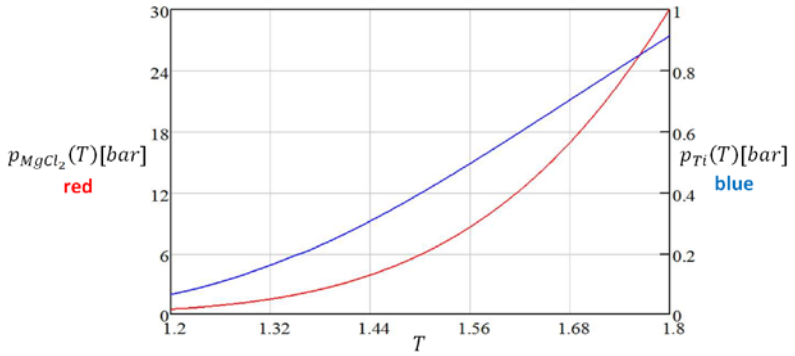

Fig. 2. Dependence of the pressure of the reaction products on the initial temperature of the reactor and magnesium.

In Fig. 1, the horizontal axis is $T[^\circ\ K \cdot 10^3]$ where T is the initial temperature of the body of the reactor where reaction (13) will proceed. It should be noted that reagent Mg initially before the reaction is at the same temperature as the body of the reactor and its mass is exactly so big to create dry saturated vapour in the volume of 30 litres of the reactor. The left vertical axis is $T_{fin}[^\circ\ K \cdot 10^3]$ (line is coloured red) where T_{fin} is the final calculated temperature of the reaction products after reaching thermodynamic equilibrium state of the products after adding to them the standard thermal effect of exothermic reaction (13). The right vertical axis is $\Delta Q(T)[MJ]$ in mega joules (line is coloured blue) where ΔQ is the thermal effect of the reaction.

In Fig. 2, the horizontal axis is $T[^\circ\ K \cdot 10^3]$, the same as in Fig. 1. The left vertical axis is the partial pressure $p_{MgCl_2}(T)[bar]$ of vapour of reaction product $MgCl_2$ (graphic is red). The right vertical axis is partial pressure $p_{Ti}(T)[bar]$ of the dry saturated vapour of reaction product titanium Ti (graphic is blue).

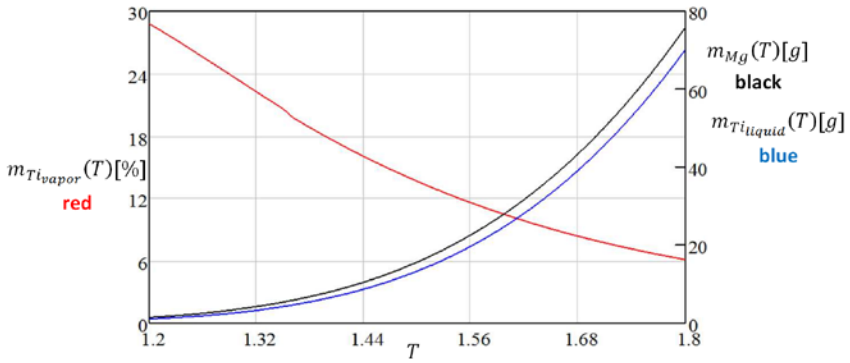

Fig. 3. Dependence of the ratio of the liquid and vapor state of titanium after the reaction on the initial temperature of the reactor and magnesium.

In Fig. 3, the horizontal axis is $T[^\circ\ K \cdot 10^3]$, the same as in Fig. 1. The left vertical axis is the mass of the dry saturated vapour of titanium as a percentage of the total mass of the titanium reduced during reaction (13) (graphic is red). The first right vertical axis is the mass of liquid titanium as percentage of the total mass of titanium reduced during reaction (13) (graphic is black). The second right vertical axis is the mass of liquid titanium as percentage $m_{Ti_{vapor}}(T)[\%]$ of the total mass of titanium reduced during reaction (13) (graphic is blue).

7. CONCLUSIONS

We have derived expression (10) that binds the temperature increase and other changes in other thermodynamic parameters of the system with a certain amount of heat that has to be added to the system in order to get the said changes. Then we have applied this equation to a situation with two substances that share the same volume, and we can do this way so far as the volume of reactor is significantly bigger than the volume of reagents and/or products of reaction in the liquid phase. Then after using pretty extensive numeric calculations, we have obtained the dependencies in graphical form for a case of the reactor volume of 30 litres and temperature range of 1200–1800 °K and presented them graphically in Figs. 1–3.

It should be noted that Fig. 3 demonstrates at first view a strange result that increasing temperature of the reactor, the vaporous part of the titanium decreases. Actually, it is the case due to our condition that titanium tetrachloride should always be injected at the same critical temperature of 638 °K.

Considering the practically achievable temperature range of the reactor body of the gaseous reaction of titanium reduction to be between 1450–1650 °K, we can estimate that at the temperature of the reactor body at 1650 °K at the end of the reaction temperature of the reaction products for even a short moment should not exceed 3600 °K and pressure should not exceed 16 bar. In order to keep the pressure at any moment in the reactor below 10 bar, the temperature of the reactor should not exceed 1500 °K.

ACKNOWLEDGEMENTS

The present research has been part of the project "Research of the Technological Process of Titanium Production" financially supported by the company ARČERS and the European Regional Development Fund, programme "Entrepreneurship and Innovation", activity 2.1.1.1. Support for Science and Research, grant No. 2014/0008/2DP/2.1.1.1.0/13/APIA/VIAA/016.

REFERENCES

1. Samsonov, G.V., Perminov V.P. (1971). Magnietermiya. M.: Metallurgy. (in Russian)
2. Wolski, A.N., Sterlin, J.M. (1967). Metallurgy of plutonium. Science. (in Russian)
3. Sergeev, V. et al. (1964). Metallurgy of titanium. M. (in Russian)
4. Vukalovic, M.P., Novikov, I. (1968). Technical Thermodynamics. M.: Energy. (in Russian)
5. Vukalovic, M.P., Novikov, I. (1972). Thermodynamics. M.: Mechanical engineering. (in Russian)
6. Morachevsky, A.G., Sladkov, I.B. (1996). Physico-chemical properties of molecular inorganic compounds. S.-Pb.: Chemistry. (in Russian)
7. Filippov, L.P. (1978). The similarity of the properties of substances. M.: MGU. (in Russian)
8. Sladkov, I.B. (2003). A simple criterion for thermodynamic similarity of molecular inorganic compounds. // *Journal of Applied Chemistry.* T.76. №12. (pp.1961-1965). (in Russian)

9. Sladkov, I.B., Hmurova, A. (1999). Predicting the temperature dependence of the enthalpy of vaporization of molecular inorganic liquids. //*Journal of Applied Chemistry*. T.72.№1. (pp. 44-48). (in Russian)
10. Reid, R. Prausnitz, J., Sherwood, T. (1977). The properties of gases and liquids. (3rd ed.) McGrawHill.
11. Reid, R. Sherwood, T. (1971). The properties of gases and liquids. Khymija, Leningrad.
12. Garmata, V.A., Petrunko, A.N., Galitsky, N.V., Olesov, G., Sandler, R.A. (1983). Titanium. M.: Metallurgy. (in Russian)

PAR GALA PRODUKTU TEMPERATŪRAS APRĒĶINA JAUTĀJUMU SLĒGTĀ APJOMĀ STRAUJI NOTIEKOŠAI EKSOTERMISKAI ĶĪMISKAI REAKCIJAI AR IEVĒROJAMU ENERĢIJAS IZDALĪŠANOS

V. Lazarevs, D. Geidmanis

K o p s a v i l k u m s

Vairāku vielu sistēmas jeb reakcijas produktu termodinamisko parametru aprēķina problēma tiek reducēta uz teorētiski stingru izohorisku termodinamisko parametru aprēķinu vienai vielai pēc zināma siltuma daudzuma pievienošanas sistēmai. Šajā rakstā mēs pamatojam viedokli, ka termodinamisko parametru izohoriskā aprēķina paņēmiens ir uzticamāks par šķietami dabisko izobārisko aprēķina veidu, jo izobāriskajā aprēķinā ir jāietver adiabātiskas saspiešanas aprēķins divfāžu sistēmas netriviālajā gadījumā, kad šķidruma – sausā piesātinātā tvaika sistēma var pāriet citā sistēmā, kurā ir termodinamisks līdzsvars starp šķidrumu un slapju piesātinātu tvaiku, kurš acīmredzot prasa ievērojami sarežģītākus aprēķinus salīdzinot ar izohorisko aprēķinu, jo vispārīgā gadījumā piesātināta tvaika īpatnējā siltumietilpība var būt negatīva.

Motivācija atrisināt šo teorētisko problēmu bija saistīta ar praktisku uzdevumu - reaktora projektēšanu, kurā augstā temperatūrā gāzveida reaģentu magnija un titāna tetrahlorīda reakcijas rezultātā tiek reducēts titāns. Šī reakcija ir pazīstama kā izteikti eksotermiska ar augstu siltuma efektu. Reakcijas gala temperatūras, spiediena un šķidrās un gāzveida fāzes reakcijas produktu sadalījuma aprēķini reaktora projektēšanas procesā ir ļoti svarīgi, piemēram, lai neļautu reakcijas produktiem iespiesties reaģentu padošanas kanālos. Pielietojot stingru teorētisku aprēķinu un izmantojot zinātniski-tehniskajā literatūrā pieejamās reakcijas produktu termodinamisko parametru vērtību heiristiskās funkcijas atkarībā no temperatūras, raksta otrajā daļā mēs uzrādām aprēķinu rezultātā iegūtās grafiskās diagrammas reakcijas beigu temperatūrai, reakcijas produktu spiedienam un šķidrās vielas un tvaika sadalījumam atkarībā no reaktora un magnija sākuma temperatūras 1200–1800°K diapazonā, kamēr titāna tetrahlorīdu vienmēr reaktorā ievada vienā un tajā pašā gāzes kritiskajā temperatūrā.

28.07.2015.

LATVIAN JOURNAL OF PHYSICS AND TECHNICAL SCIENCES
2016, N 1

DOI: 10.1515/lpts-2016-0006

SOLID STATE PHYSICS

SYNTHESIS OF GRAPHENIC CARBON MATERIALS ON NICKEL PARTICLES WITH CONTROLLED QUANTITY OF CARBON

V. Grehov[1*] , J. Kalnacs[1**] , A. Mishnev[2], K. Kundzins[3]
[1] Institute of Physical Energetics, 21 Aizkraukles Str., Riga, LV-1006, LATVIA
[2] Latvian Institute of Organic Synthesis,
21 Aizkraukles Str., Riga, LV-1006, LATVIA
[3] Institute of Solid State Physics, University of Latvia,
8 Kengaraga Str., Riga, LV-1063, LATVIA

A cheap, comparatively simple and effective method is proposed for the large quantity production of the sheets of graphenic carbon materials (GCM) by annealing the mixture of nickel powder with a suitable carbon amount at the temperatures close to 1000 ºC. The number of graphene layers in the sheets of GCM may be varied by altering the amount of carbon in the mixture and parameters of annealing and drying of the obtained products. Samples of GCM were prepared in the form of heat-dried GCM paper and in the form of graphene sponge with freeze-drying. The appearance of GCM on the surface of Ni particles was identified using a scanning electron microscope (SEM) at a low accelerating voltage of 5 kV. The thickness and properties of the layers were investigated by electron microscopy and X-ray diffraction. The fabrication processes were carried out at the concentrations of added carbon from 0 to 1 at%. The results obtained are fully consistent with the well-known solid phase reactions of carbon dissolution in Ni at 1000 °C and graphene or graphite precipitation on the surface with cooling down to the room temperatures.

Keywords: *graphene structures, few layers graphene sheets, carbon*

1. INTRODUCTION

Graphene, a 2D carbon allotrope, has drawn significant interest among scientists due to a number of intriguing properties [1]–[4].

The methods for graphene production, excluding mechanical exfoliation [1], can be divided into two groups: chemical cleavage, including the step of graphite oxidation [5], [6]; and the methods for dosed position of carbon atoms on the substrate where under certain conditions graphene is formed [7]–[11].

The chemical cleavage methods provide graphene in considerable quantities; however, the quality of such graphene is rather poor, since it usually contains

* Corresponding author. Tel: 0037128253782. E-mail: v.v.grehov@gmail.com (V.Grehov)
** Corresponding author. Tel: 0037126321168. E-mail: jkalnacs@edi.lv (J. Kalnacs)

oxygen-containing groups [5], [6]. High-quality graphene with a large area can be prepared on substrates of a catalytic transition metal – such as Ni or Cu – by thermal chemical vapour deposition (CVD) [7], [8]. Good quality graphene and direct control of the number of layers are achieved using the methods of the dosed deposition of amorphous carbon under the layer of Ni catalyst on Si/SiO_2 substrate [9], ion implantation of carbon clusters in the Ni catalyst layer [10], and pulsed laser carbon deposition [11]. Graphene can also be obtained using Ni powder as a catalyst in the thermal decomposition of SiC powder [12] and by pyrolysis of poly(methyl methacrylate) on particles of Ni powder [13].

The aim of the present research has been to create a simple and available method for production under the laboratory conditions of graphenic carbon materials (GCM) which consist of sheets (flakes, plates) with a predefined number of graphene layers.

GCM particles may be as 2D graphene materials (graphene, multilayer graphene (MLG) with the number of layers <10) and 2D graphite materials (graphite nanoplates or sheets with the thickness of <100 nm), as well as bulk graphite.

2. EXPERIMENTAL SECTION

Our method for producing GCM is based on the well-known solid phase reaction of carbon dissolution in nickel at high temperatures and graphene precipitation on the surface of nickel with cooling to the room temperature (RT) [14]. For GCM production a special nickel-carbon powder mixture was heated in inert atmosphere to a temperature of 900–1000 °C and cooled to RT. The carbon material was extracted from the mixture and studied using scanning (SEM) and X-ray diffraction (XRD). As a result, a significant portion of the carbon material was transformed into GCM.

For dissolution of carbon and precipitation of GCM, as the catalyst the commercial Ni powder (purity 99.8 %, the main grain size ~ 10 μm) was chosen. On this catalyst, GCM was successfully obtained from methane by chemical vapour deposition (CVD) method [15]. As the source of carbon, Carbopack X powder (Sigma-Aldrich) was taken. The choice of initial materials in form of powders gave us the possibility to vary composition of mix and, as initially was supposed, the GCM sheet thickness. During the research, it was found that Ni raw powder contained carbon as an impurity. The carbon concentration of the starting powder was determined by dissolving Ni powder and carbon residue weighed after filtering the solution. The obtained values were 0.043 wt% or 0.21 at%.

Mixing of Ni powder with appropriate amount of carbon was carried out by ball milling for 30–35 min at the mix and ball weight ratio 1:4.

The first series of experiments was done manually [16]. The annealing of the quartz cuvette with 40 g of mix Ni-C was carried out in a horizontal movable quartz pipe of tubular furnace. The cuvette was loaded in the working zone of furnace and the pipe was pumped out to $5 \cdot 10^{-3}$ bars; then Ar and H_2 flows (400 ml/min and 50 ml/min, respectively) were let in, and after furnace heating up to 400–600 ºC the cuvette was kept for 30 min. Further, heating up to 900–1000 ºC and 12–80 min annealing proceeded in the flowing atmosphere of Ar (400 ml/min). Cooling down to RT took

place in the Ar atmosphere – either fast (~ 200º/min, outside the furnace) or slowly (~ 1–5º/min inside the furnace).

The second series of experiments carried out on the thermogravimeter SET-SYS-1750 (Setaram, France) allowed us to automatically carry out processes with programmed sequences of gas flows and furnace temperatures. The 3 g of Ni-C mix in the alumina crucible (1300 mkl) was placed in a vertical furnace of SET-SYS-1750. After air evacuation from the furnace, the flow of Ar and H_2 of 200 and 10 ml/min, respectively, through the furnace was started. The furnace temperature was raised to 200–450 °C at a rate of 8–20 °C/min, and aged for 0.5–1 h.

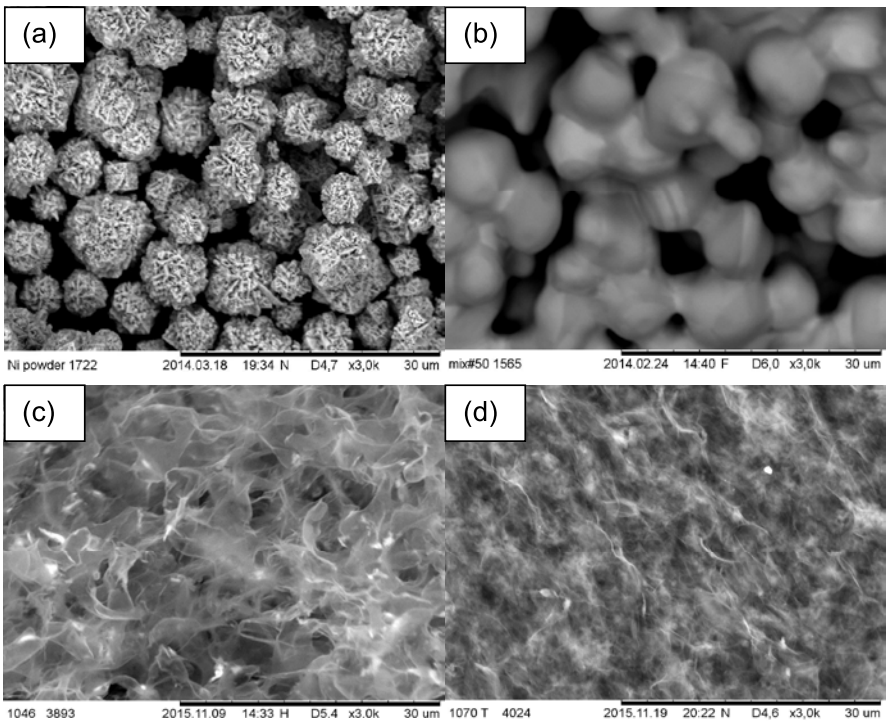

Fig. 1. SEM image of the initial Ni powder particles (a) and after annealing with the added carbon (b). GCM sheets are seen on the particle surface as dark covering on light particles. GCM sheets after removal of Ni and freeze-drying (c) (1049 mix070) the GCM sponge or after thermo-drying (d) (1053 mix070) the GCM paper.

Then, the flow of H_2 was reduced to 2ml / min; the furnace temperature was raised to 950–1000ºC at a speed of 7–20 °C / min and maintained for 0.5–1 hour. Fast cooling of the sample took place in the furnace, while the heater was off and the coolant was circulated. In the beginning, the cooling rate reached 65 °C per minute. Time for cooling to 500 °C was less than 9.5min. Slow cooling rate was 2 °C / min.

Mode programmable experiment (400/1000) means temperature of the first heating in the presence of hydrogen and the second heating in a stream of argon. The heating rate was 20 ºC per minute. Warm-up time at the elevated temperature was 1 hour in both cases.

At high temperatures, the sintering of the individual particles of Ni powder by evaporation of Ni atoms from the tips of convex sites and deposition of Ni atoms into the concave sections (in places of contact) particles take place. All particles become connected, and the powder sinters forming an ingot. The initial Ni powder and Ni powder with added carbon after heat treatment are shown in Fig. 1 (a), (b). On the surface of Ni sheets, GCM are seen as dark strips and rings. The contrast between these surfaces with and without GCM can be observed at a low SEM acceleration voltage (5 kV) [17], [18].

Freestanding GCM sheets were obtained after dissolution of the Ni ingot in diluted to 7 wt% nitric acid, with stirring and heating up to 70 ºC. In the course of Ni ingot dissolution, the GCM covering seen in Fig. 1(b) could disintegrate into separated GCM sheets, or linkages between the GCM sheets which emerged at their formation could remain. In the first case, GCM samples were obtained by vacuum filtration of the etchant containing GCM through a nitrocellulose membrane filter with a pore size of 1.2 μm. After such filtration, GCM samples were washed with distilled (DI) water and dried at 100 ºC; then GCM was separated from the membrane in the form of a ***GCM paper*** (Fig. 1(d)). Some samples were so thin that could not be removed from the filter; they were investigated as a ***layer of GCM on the filter***. In the second case, a carbon body remained in etchant in the form of the original ingot and then it was boiled in DI water (three times) and dried or by heating between two membranes under small load or this wet carbon body was frozen and dried by vacuum sublimation of water at the temperatures from -10 ºC to -3 ºC. After thermal drying, carbon body samples were looking like the GCM paper samples. After freeze-drying carbon body samples had the form of ***GCM sponge*** [19] (Fig. 1(c) and Fig. 2 (c, d)).

Appropriate GCM samples were analysed by means of SEM (Hitachi TM3000), high resolution SEM LYRA3 XMU (Tescan, Czech Republic) and XRD (Japan Rigaku ULTIMA IV, Cu–Ka radiation $\lambda = 0.154184$ nm).

The thickness of these sheets was estimated by Scherrer's equation [20] from the XRD (002) peak broadening (Fig. 3). All calculations were done with Scherrer's scale factor 0.9.

From Fig. 1(c) it is seen that the GCM sponge consists of randomly placed freestanding GCM sheets. Individual GCM sheets have a bend and shape similar to the dark covering on the particles of Ni powder after annealing (Fig. 1 (b)).

Samples in the form of GCM paper consist of randomly aggregated crumpled sheets closely linked to each other. In Fig. 1 (d), the single graphene sheets are distinguished and under them the alternation of light and dark areas can be seen. They are the separate sheets of graphene which are corrugated in lumps. Bright areas are less conductive; they probably have some excess charge.

Observations of the structure for thermally dried GCM samples by high resolution transmission electron microscope (HRTEM) [21] confirmed that our samples contained MLG sheets. Our thermally dried GCM samples by SEM with high resolution [21], as well as samples with freeze-drying are shown in Fig. 2. The graphene sheets crumpled in lumps are shown with arrows. We believe that all the pieces of light material in Fig. 1 (d) and Fig. 2 (a) are graphene sheets crumpled in clumps like those shown by arrows in Fig. 2. Clumping of graphene sheets begins in the step of

etching nickel from the disintegration of the carbon coating onto individual sheets and flakes in suspension in acid solution or in water. While maintaining the carbon body in ingot form this does not happen.

The density of GCM sponges determined from the ratio of the weight in a dry state with respect to the wet weight (after boiling in water) gives the values of 10–14 mg / cm^3.

3. RESULTS AND DISCUSSION

To perform some preliminary estimates on how much carbon was required in the mix, we proceeded with simple geometrical considerations in particular, the Ni powder was considered as a sum of identical spherical particles with size of 10 μm in diameter. This size was chosen based on SEM observations. Assuming that all carbon dissolves in the volume of Ni particles at heating and precipitates on their surfaces when cooling, it was easy to calculate the carbon concentration required for obtaining a definite number of graphene layers on these surfaces. The maximum carbon concentration is estimated by its solubility at different heating temperatures. At heating up to 1000 ºC this concentration is up to 1.2 at% according to the temperature dependence of carbon solubility in Ni [14]. For such concentration of carbon in the initial mix, in an ideal case it is possible to form a GCM with 50 layers on all surfaces of Ni particles with diameter of 10 μm.

In practice [14], [18], [22], [23], [24], the GCM structures which are grown on polycrystalline Ni surface are not uniform in thickness. The non-uniformity of thickness occurs due to the presence of two different ways of graphene growth on the Ni surface. Monolayer or bilayer graphene on the polycrystalline Ni usually grows on the surface of large Ni grains with (111) or (011) orientation [18] and the absence of grain boundaries (i). In this case, carbon precipitates to the surface by diffusion of Ni directly through bulk Ni.

In contrast, graphene formed near the grain boundaries for the most part is multilayer graphene, and grain boundaries serve as nucleation sites for multilayer graphene growth (ii). Escape of carbon atoms on the surface occurs through the favourable domain boundaries, which in the places of entrance to the surface form the nucleation sites for multilayer graphene growth along the Ni surface [25]. It should be noted that some grain boundaries act as a fast diffusion path or enhanced local carbon sources in comparison with diffusion through the bulk Ni.

For limiting the heterogeneity of graphene coating by CVD, several steps were taken to improve the structure of the deposited polycrystalline nickel substrate – for the approximation to the Ni single crystal structure [25]. The resulting coating was epitaxially grown graphene with areas up to 1 mm. It was topped with the individual multilayer sheets arranged turbostratically relative to epitaxial graphene. Locations of sheets were above the twin boundaries in the nickel substrate.

Another approach for limiting the heterogeneity of graphene in the CVD method is based on suppression of carbon diffusion through the grain boundaries. For this purpose, after carburizing Ni with CH_4 the substrate temperature rises under H_2 to a segregation temperature (onto 50 Cº above) [26]. This results in dissolution

and removal of disordered graphene layers on the Ni surface.

In the present research, we assumed that in the case of annealing powder mixtures with various dose of carbon a regime might be found when the average value of thickness of GCM layers would depend on the amount of carbon in the initial Ni-C mix. It should be noted that the average value of thickness corresponds to real thickness, if the main growth of GCM layers occurs fiberwise on domains (111) during the diffusion directly through bulk Ni [24], [26].

In Fig. 4, the XRD curves for GCM samples are given. It is known that the width of diffraction (002) maximum for graphite is determined by the crystallite size in the direction of C axis [20], which in the case of GCM layers is its thickness and defines the number of graphene layers in it.

For thickness determination by Scherrer's equation, the diffraction peak (002) was approximated by the Voigt or Gauss profile using standard software (X'Pert HighScore or Origin 8.6). The obtained diffraction peaks were asymmetric, which was seen as an increase in the peak width at lower angles. A similar asymmetry in the case of carbon nanostructures is associated with heterogeneity of the studied substance, e.g., when there is partial oxidation [27], disordered graphite planes and/or amorphous sites [28]. Approximation of such peaks by a symmetrical profile can give some effective GCM sheet thickness (Fig. 4 (a)). In some cases, distortions of the diffraction peak clearly indicate the presence of sample material in two components: the less ordered, thin (<1nm) layer, giving a broad peak (10–15º) and thick (about 10 nm) layer GCM giving a narrow peak (~ 1º) (Fig. 4(b)).

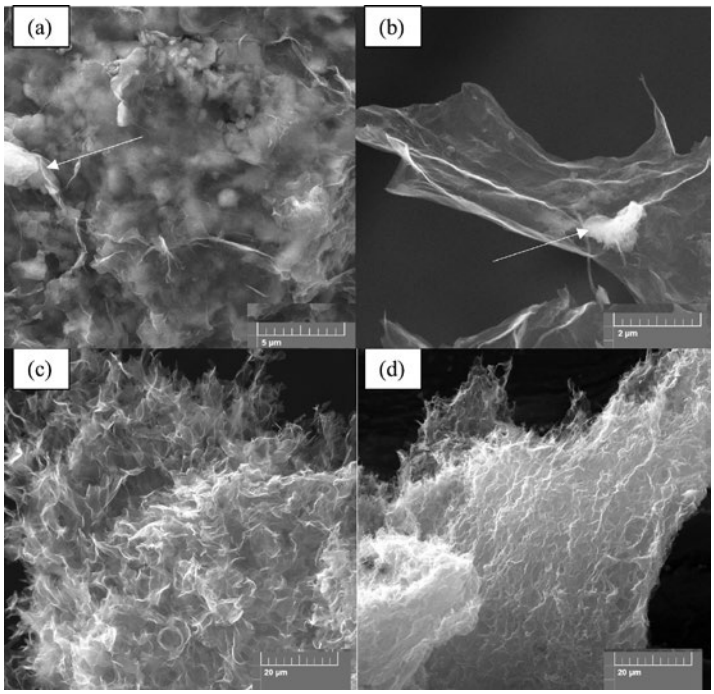

Fig. 2. High-resolution SEM images of (a) – GCM thermo dried sample (#31) in form of graphene paper with some particles on the surface (indicated with arrow); (b) – freely suspended GCM sheets with some particles on the surface (indicated with arrow), (c, d) – GCM samples (1037) and (1052) in form of GCM sponges.

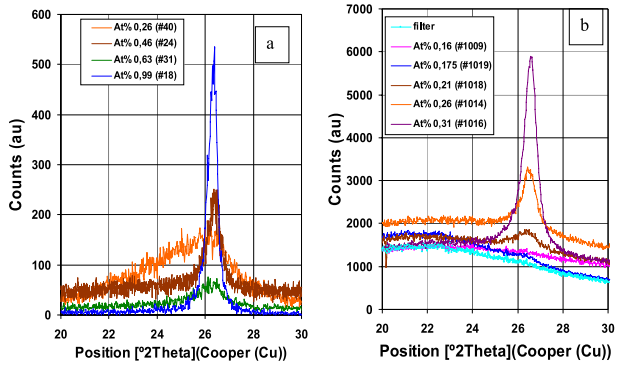

Fig. 3. XRD patterns of the GCM samples after Ni dissolution, (a) – for manual experiments in tubular furnace (GCM paper), and (b) – for programmed experiments (400/1000) in the Setaram furnace (GCM layers on the filter).

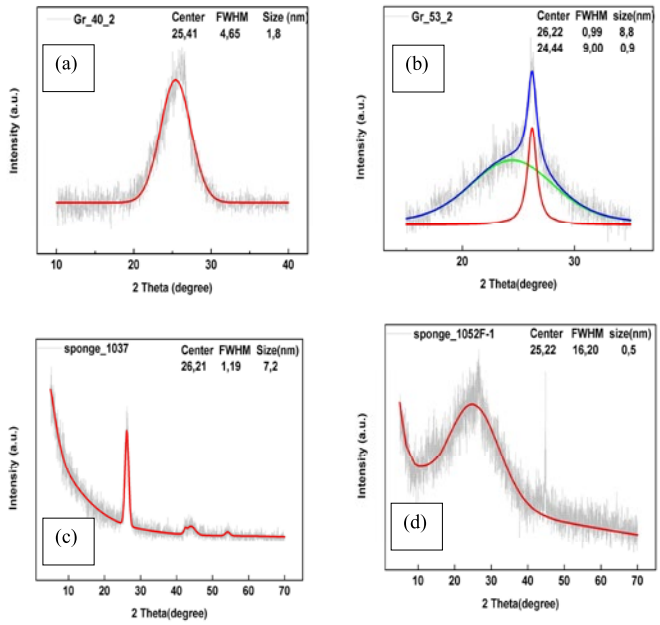

Fig. 4. XRD patterns of the GCM samples, (a) – GCM paper (#40_2), (b) – (GCM paper #53_2), (c) – GCM sponge (1037), (d) – GCM sponge (1052F-1).

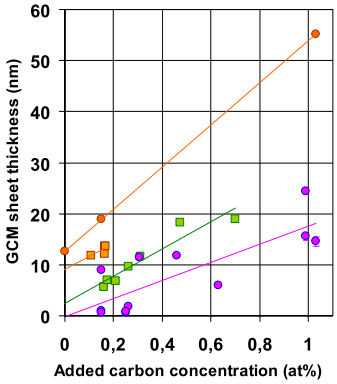

Fig. 5. Thickness of GCM layers vs. concentration of the added carbon for different annealing regimes. Orange colour: slow-cooling samples. The point corresponding to the zero carbon concentration is obtained without carbon addition. Magenta colour: fast-cooling samples made in furnace in different manual regimes. Green colour: samples made in Setaram TG furnace in (400/1000) regime with fast-cooling. Lines: a linear fit of the data. All samples were thermo-dried after water rinse and investigated in the form of GCM paper.

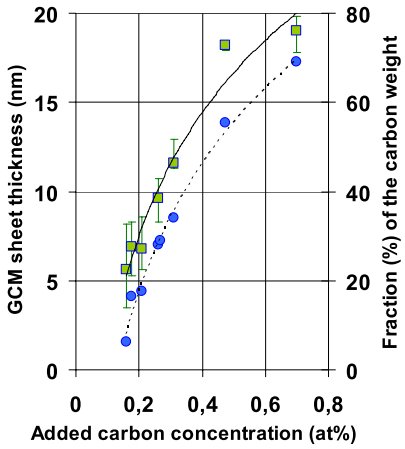

Fig. 6. Green squares – thickness of GCM layers vs. concentration of the added carbon for samples made in Setaram TG furnace in the program regime (400/1000) with fast-cooling and thermo drying after water rinse; blue circles – fraction of output carbon weight to the initial carbon weight before annealing. Samples are investigated in the form of GCM paper.

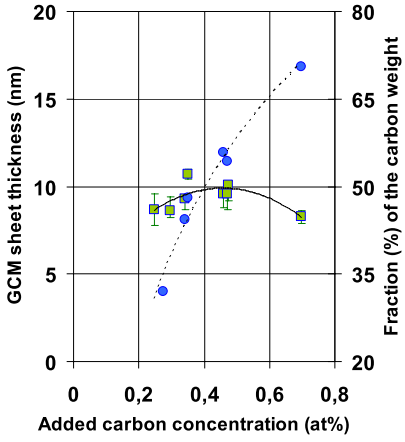

Fig. 7. Green squares – thickness of GCM layers vs. concentration of the added carbon for samples made in Setaram TG furnace in the program regime (400/1000) with fast-cooling and freeze-drying after water rinse; blue circles – fraction of output carbon weight to the initial carbon weight before annealing. Samples are investigated in the form of GCM sponge.

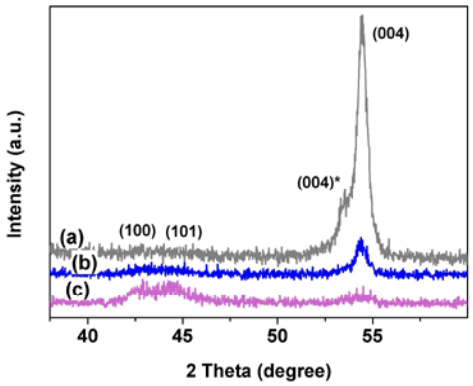

Fig. 8. XRD patterns of three GCM samples (a) (_1053-1) – programmed regime (400/1000) with added carbon 0.7 at %, thermo dried; (b) (_18-10-80) – manual with nearly the same regime, added carbon 1.0 at % and thermo dried; (c) (_1049-5-70) – programmed regime with all parameters as it is for sample (a), but with freeze-drying. All samples with rapid cooling rates.

In Fig. 5, the thickness of GCM sheets is shown depending on the concentration of the added carbon in the processes which after water rinse were thermo-dried. The large deviation of GCM sheet thickness from the common trend line (Fig. 5, magenta circle) is connected with variation in time and temperature in the first annealing in the H2 flow and final annealing in Ar in manual processes.

In Fig. 6, data points of GCM sheet thickness for programmed experiments (green squares) are shown, with data points for carbon weight output fraction to the initial carbon weight, for which the last operation was thermo- drying (blue circuits). GCM sheet samples with thermo-drying have the tendency of thickness growth with increasing concentration of added carbon. This trend is not stored for samples in the form of a GCM sponge which can be obtained in the same programme regime, only drying from water takes place by freezing and sublimation (Fig. 7 – green squares). The thickness of these samples changed slightly between 8 and 11 nm, with a change in the dosage of added carbon from 0.25 to 0.7 at%. In the both cases, the weight fraction of obtained GCM was growing identically from 10 % to 70 % by increasing added carbon concentration from 0 to 0.8 at% (Figs. 6, 7 – blue circles). The sample of these GCM sponges is shown in Fig. 1 (c) and Fig. 2 (c). This result casts doubt on the determination of the thickness of GCM layers formed on the surface of nickel powder by measuring the width of the peak (002) on the X-ray diffraction patterns for the samples have passed the stage of thermal drying. Evaporation of water from the liquid phase during heat drying causes contraction inside pairs of individual sheets due to surface tension of water and further gluing them by the van der Waals forces. This causes an increase in thickness of the individual sheets or in some areas of the sheets. The degree of restacking of sheets with nearly equal thicknesses is proportional to their number or common square or output carbon weight, that grows along with the concentration of carbon in the initial mix. That is the reason of thickness dependence of GCM sheets vs. initial concentration of carbon. In contrast to thermal drying, freeze-drying does not lead to such a drastical change in the morphology of the GCM samples.

The thickness values derived from the X-ray spectra are the actual thickness of the GCM layers formed on the surface of the nickel powder (Fig. 7 – green squares). Please note that a slight change in the morphology may occur during freeze-drying, and especially for the thinnest layers of GCM. From the above, it can be assumed that in this (400/1000) regime of annealing the thickness of the layers obtained at different quantity of carbon in the initial mix may be connected with the growth of layers on the grain boundaries as nucleation sites which form a step with height of 8–10 nm. It is the reason why the thickness of layers is almost the same and only the area or weight of the sheets grows (Fig. 7). Roughness of this size is typical of polycrystalline layers of nickel [24]. This result indicated that graphene growth on the surface of Ni powder particles was determined by the roughness of its surface.

To limit roughness, the heating rate [24] was reduced to 8 ºC/ min, the temperature of preheating in H_2 was increased to 470 ºC [29], and the temperature of the annealing was reduced to 930 ºC. For this mode of annealing with last operation of freeze-drying GCM sponges were obtained with a small number of layers (See Fig. 2 (d), and Fig. 4 (d)). The number of layers was estimated as 3 by comparing with Fig. 5 from [30].

For Fig. 5(a) it should be noted that the thickness of GCM sheets obtained in slow-cooling processes is always greater than that of GCM sheets obtained in fast cooling at the same concentration of the added carbon (Fig. 5(a), orange points). The reason may be related to a limited rate of diffusion of carbon in nickel, which does not allow precipitating all of the carbon to the surface of nickel particles from

particle volume in case of fast (non-equilibrium) cooling. It can be understood as follows: At high temperatures, the diffusion length of carbon in nickel is large, but the solubility of carbon in nickel is high and there is no excess concentration for separation on the surface. When cooling down to the temperature at which the concentration of dissolved carbon exceeds its solubility, the carbon starts precipitating on the nickel surface. Excessive concentration occurs at a lower temperature but the length of the diffusion of carbon reduces. It can be shown that at a fast cooling rate a considerable part of carbon would not escape from the bulk of Ni due to restriction of near-surface area by decreased diffusion length and reduced time for this process. All the arguments mentioned above can be attributed to the growth of GCM layers in the both variants (i, ii). The obtained data allow suggesting that at a high cooling rate the precipitation of carbon with GCM formation comes from the near-surface area of nickel particles, while at a slow cooling rate – from the entire bulk of Ni particles.

The relationship between the thickness of GCM sheets and the cooling rate becomes more complicated due to the recrystallisation of the surface of Ni particles in the cooling stage towards the orientation (111) and decrease in the number of nucleation sites of multilayer graphene on the film [29].

The presence of the (100) and (101) peaks in Fig. 8 is indicative of crystalline regions with "AB" structure in the sample [31]. The width of peak (100) in Fig. 8 (c) gives an estimate of the longitudinal crystallite size La ~ 1-1.2 nm in GCM sheets of sample.

The spectra shown in Fig. 8 were obtained on samples with approximately the same manufacturing conditions. The main difference was in the method of drying after washing with water: thermal drying (a), (b) and freeze-drying (c). Figure 8 (a, b) in the diffraction peak (004) for thermally dried samples dominates over the peaks (100) and (101). This suggests that in these samples the (ab) plane with respect to the specimen (plate) has the preferred direction. The sample with randomly spaced individual sheets of GCM (volumetric the spongy body Fig. 1 (c) and Fig. 2 (c, d)) has a predominance of diffraction peaks (100) and (101) corresponding longitudinally along the plane of the graphene sheets. The preferred direction for the samples in the thermal drying under a light load may be related to the bonding of adjacent GCM sheets. The thickness of the layers will be increased (Fig. 6) and on the diffraction peak (004) shoulder (004*) appears (see Fig. 8 (a)) associated with an increase in the interplane distances in the field of accidental connection of separate GCM sheets.

Presence of this shoulder means that the GCM samples contain regions of turbostratic-like structure in which the individual sheets are rotated relative to the adjacent graphene sheets at an arbitrary angle. The analysis of data in Fig. 8 (a), (b) shows that the centre of peak 004 corresponds to d 004 = 1.68 Å, i.e. to graphite, while for the centre of additional peaks (004*) the distance d 004* = 1.70–1.72 Å is equal to the interplanar d_{004} distance of turbostratic graphite [32]. Note that the centre of peak (004) for graphene sponge with randomly spaced individual sheets corresponds to 1.68 Å of interplanar spacing and absent additional peak (Fig. 8 (c)). It should be noted that turbostratic packaging of graphene layers in the MLG grown on polycrystalline nickel is often shown by electron diffraction [25].

4. CONCLUSIONS

The approach to synthesis of GCM sheets on nickel particles by mix of Ni powder with carbon powder proposed in the present research has been tested. In the experiments, GCM were obtained in the form of graphene sponge and/or paper. It has been shown that thermal drying of GCM samples after water rinse leads to significant changes in the morphology of the GCM samples. The bonding of GCM individual sheets occurs. The thickness of the sheets increases and peak (002) width decreases in the X-ray spectra. The additional peak (004*) appears near the peak (004), which corresponds to an arbitrary (rotated) position of glued GCM sheets and an increased interplanar distance.

Structurally, our GCM consist of nanocrystalline sheets with a size of crystallites about of 10 nanometres (Fig. 8 (c)), at the external sizes up to 1–10 μm (Fig. 1 (c) and Fig. 2 (b), (c), (d)).

For the mode of annealing (400/1000) for Ni-C mixture, it has been shown that the mechanism of growth is associated with the grain boundaries of crystallites having a step about 8–11 nm. The GCM sponges with sheets of this thickness were obtained.

For special mode of annealing, the GCM sponges with a small number of layers (~3) were obtained (Fig. 2 (d)).

Controlling the surface roughness by annealing regime change and variation, the amount of added carbon can further lead to GCM sponge with a predetermined number of layers.

In compliance with the method presented, GCM sponges with a different number of layers can be prepared and used as sensors, contacts for supercapacitors, adsorbents, thermal conductors that can give a lot of perspective applications.

ACKNOWLEDGEMENTS

The present research has been supported by the National Research Programme for 2014–2017 "Multifunctional Materials and Composites, Photonics and Nanotechnologies".

REFERENCES

1. Novoselov, K.S., Geim, A.K., Morozov, S.V., Jiang, D., Zhang, Y., Dubonos, S.V., et al. (2004). Electric field effect in aAtomically thin carbon films. *Sci 2004*:306, 666–9.
2. Batzill, M. (2012). The surface science of graphene: Metal interfaces, CVD synthesis, nanoribbons, chemical modifications, and defects. *Surface Science Reports 2012*: 67, 83–33.
3. Singh, V., Joung, D., Zhai, L., Das, S., Khondaker, S.I., and Seal, S. (2011). Graphene based materials: Past, present and future. *Progress in Materials Sci 2011*:56, 1178–94.
4. Avouris, P., and Dimitrakopoulos, C. (2012). Graphene synthesis and application. *Materials Today 2012*: 15(3), 86–11.
5. Wang, S.J., Geng, Y., Zheng, Q., and Kim, J.K. (2010). Fabrication of highly conducting and transparent graphene films. *Carbon 2010*:48, 1815–8.

6. Yuana, W., Li, B., and Li, L. (2011). A green synthetic approach to graphene nanosheets for hydrogen adsorption. *App Surf Sci 2011*:257, 10183–4.
7. Yu, Q.K., Lian, J., Siriponglert, S., Li, H., Yong, Chen P.Y., and Pei, S.S. (2008). Graphene segregated on Ni surfaces and transferred to insulators. *Appl phys lett 2008*: 93, 113103–3.
8. Liu, W., Li, H., Xu, C., Khatami, Y., and Banerjee, K. (2011). Synthesis of high-quality monolayer and bilayer graphene on copper using chemical vapor deposition. *Carbon 2011*:49, 4122–8.
9. Zheng, M., Takei, K., Hsia, B., Fang, H., Zhang, X., Ferralis, N., et al. (2010).Metal-catalyzed crystallization of amorphous carbon to graphene. *Appl Phys Lett 2010*: 96(6), 063110–3.
10. Wang, G., Ding, G., Zhu, Y., Chen, D., Ye, L., Zheng, L., Zhang, M., Di, Z., and Liu, S. (2013). Growth of controlled thickness graphene by ion implantation for field-effect transistor. *Materials Lett 2013*: 107, 170–3.
11. Koh, A.T. T., Foong, Y., M., and Chua, D., H. C. (2012). Comparison of the mechanism of low defect few-layer graphene fabricated on different metals by pulsed laser deposition. *Diamond & Related Materials 2012*:25, 98–4.
12. Li, D., Zeng, X., Yang, Y., Yang, J., and Yuan, W. Freestanding graphene in large quantity prepared by Nickel catalyzed decomposition of SiC powder. *Materials Lett 2012*: 74, 19–3.
13. Hong, N., Yang, W., Bao, C., Jiang, S., Song, L., and Hua, Y. (2012). Facile synthesis of graphene by pyrolysis of poly(methyl methacrylate) on nickel particles in the confined microzones. *Materials Research Bull 2012*:47, 4082–6.
14. Baraton, L., He, Z. B., Lee, C. S., Cojocaru, C. S., Chatelet, M., Maurice J. L., Lee Y. H., and Pribat, D. (2011). On the mechanisms of precipitation of graphene on nickel thin films. *European Phys Lett 2011*: 96, 46003–6.
15. Chen, Z., Ren, W., Liu, B., Gao, L., Pei, S., Wu, Z.–S., Zhao, J., and Cheng, H.–M. Bulk growth of mono-to few-layer graphene on nickel particles by chemical vapor deposition from methane. *Carbon 2010*: 48, 3543 –7.
16. Grehov, V., Kalnacs, J., Vilken, A., Mishnev, A., Chikvaidze, G., Knite, M., and Saharov, D. (2014). Graphene nanosheets grown on Ni particles. *Joint symposium RCBJSF-2014-FM&NT*. Book of Abstracts, 303.
17. Gupta, A.K. (2009). Raman Scattering from n-Graphene Layers [dissertation]. The Pennsylvania State University: The Graduate School, Department of Physics, 50–3.
18. Takahashi, K., Yamada, K., Kato, H., Hibino, H., and Homma, Y. (2012). In situ scanning electron microscopy of graphene growth on polycrystalline Ni substrate. *Surface Science 2012*: 606, 728–4.
19. Inagaki, M., Qiu, J., and Guo, Q. (2015). Carbon foam: Preparation and application. *Carbon 2015*: 87, 128–24.
20. Iwashita, N., Park, C. R., Fujimoto, H., Shiraishi, M., and Inagaki, M. (2004). Specification for a standard procedure of X-ray diffraction measurements on carbon materials. *Carbon 2004*:42, 701–13.
21. Grehov, V., Kalnacs, J., Vilken, A., Mishnev, A., Knite, M., and Kundzins, K. (2015). Structural investigation of graphenic carbon materials obtained on nickel particles. *FM&NT-2015 Functional Materials and Nanotechnologies.* Book of Abstracts, 115.
22. Obraztsov, A. N., Obraztsova, E. A., Tyurnina, A. V., and Zolotukhin, A. A. (2007). Chemical vapor deposition of thin graphite films of nanometer thickness. *Carbon 2007*:45, 2017–4.

23. Reina, A., Jia, X., Ho, J., Nezich, D., Son, H., Bulovic, V., Dresselhaus, M.S., and Kong, J. (2009). Large area, few-layer graphene films on arbitrary substrates by chemical vapor deposition. *Nano Lett 2009*: 9, 30–5.
24. Zhang, Y., Lewis Gomez, L., Ishikawa, F. N., Madaria, A., Ryu, K., Wang, C., Badmaev, A., and Zhou, C. (2010). Comparison of graphene growth on single crystalline and polycrystalline Ni by chemical vapor deposition. *J Phys Chem Lett 2010*:1, 3101–6.
25. Fogarassya, Z., Rummelib, M. H., Gorantlad, S., Bachmatiukb, A., Dobrika, G., Kamarase, K., Laszlo, P. B., Havancsak, K., Labar, J. L. (2014). Dominantly epitaxial growth of graphene on Ni (111) substrate. *Appl Surf Sci 2014*:314, 490–9.
26. Gong, Y., Zhang, X., Liu, G., Wu, L., Geng, X., Long, M., Cao, X., Guo, Y., Li, W., Xu, J., Sun, M., Lu, L., and Liu, L. (2012). Layer-controlled and wafer-scale synthesis of uniform and high-quality graphene films on a polycrystalline nickel catalyst. *Adv Funct Mater 2012*: 22, 3153–6.
27. Hu, H., Zhao, Z., Zhou, Q., Gogotsi, Y., and Qiu, J. (2012). The role of microwave absorption on formation of graphene from graphite oxide. *Carbon 2012*:50, 3267–6.
28. Kicinski, W., Norek, M., and Bystrzejewski, M. (2013). Monolithic porous graphitic carbons obtained through catalytic graphitization of carbon xerogels. *J of Phys and Chem of Solids 2013*: 74, 101–8.
29. Reina, A., Thiele, S., Jia, X., Bhaviripudi, S., Dresselhaus, M. S., Schaefer, J.A., and Kong, J. (2009). Growth of large-area single- and bi-layer graphene by controlled carbon precipitation on polycrystalline Ni surfaces. *Nano Res 2009*: 2, 509–7.
30. Tu, Z., Liu, Z., Li, Y., Yang, F., Zhang, L., Zhao, Z., Xu, Ch., Wu, S., Liu, H., Yang, H., and Richard, P. (2014). Controllable growth of 1–7 layers of graphene by chemical vapour deposition. *Carbon 2014* 73, 252–6.
31. Fujimoto, H. (2003). Theoretical X-ray scattering intensity of carbons with turbostratic stacking and AB stacking structures. *Carbon 2003*: 41, 1585–7.
32. Букалов, С. С., Михалицын, Л. А., Зубавичус, Я. В., Лейтес, Л. А., Новиков, Ю. Н. (2006). Исследование строения графитов и некотрых других sp2 углеродных материалов методами микроспектроскопии КР и рентгеновской дифрактометрии. *Рос Хим ж 2006*: L(1), 83–8.

GRAFĒNA STRUKTŪRU IZVEIDE UZ NIKEĻA GRAUDIEM AR KONTROLĒJAMU OGLEKĻA SATURU

V.Grehovs, J. Kalnačs, A. Mišņevs, K. Kundziņš

K o p s a v i l k u m s

Grafēna oglekļa struktūras sintezētas uz niķeļa pulvera ar graudu lielumu ap 10 mikronu. Atkarībā no gatavo struktūru žāvēšanas veida iegūtas divas formas – brīvi izvietots multislāņu grafēna "papīrs", vai grafēna sūkļveida struktūras ar dažu grafēna kārtiņu biezumu. Iegūtās struktūras pētītas ar rastra elektronu mikroskopu, augstas izšķirtspējas caurstarojošo elektronu mikroskopu un rentgenstaru difrakciju.

Iegūtie grafēna slāņi ir nanokristāliski ar graudu lielumu 1 – 10 nanometri. Sūkļveida struktūras ir ļoti perspektīvas kā absorbenti, tās tiek pielietotas superkondensatoros, sensoros u.c.

07.01.2016.

LATVIAN JOURNAL OF PHYSICS AND TECHNICAL SCIENCES
2016, N 1

DOI: 10.1515/lpts-2016-0007

APPLIED PHYSICS

TRIBOLOGICAL PROPERTIES OF PVD CARBON-COPPER COMPOSITE FILMS REINFORCED BY TITANIUM

J. Lungevics[1], A. Leitans[1], J. Rudzitis[1], N. Bulahs[1], P. Nazarovs[2], V. Kovalenko[2]

[1]Institute of Mechanical Engineering,
Riga Technical University,
6 Ezermalas Str., LV-1006, Riga, LATVIA
E-mail: mti@rtu.lv

[2] LTD Naco Technologies
24A-52 Ganibu dambis, LV-1005, Riga, LATVIA
E-mail: info@nacotechnologies.com

Carbon-copper composite coatings reinforced with titanium were deposited using high power magnetron sputtering technique. Tribological and metrological tests were performed using Taylor Hobson Talysurf Intra 50 measuring equipment and *CSM Instruments* ball-on-disk type tribometer. Friction coefficient and wear rate were determined at 2N, 4N, 6N loads. It was revealed that friction coefficient decreased at a higher Ti concentration, which was particularly expressed at bigger applied loads. However, wear volume values tended to increase in the beginning, till Ti concentration reached about 11 %, but then decreased, thus providing better nanocoating wear resistance.

Keywords**:** *3D roughness, carbon-copper composite, magnetron sputtering, nanocoatings, solid lubricant, wear.*

1. INTRODUCTION

Many enterprises that specialise in mechanical engineering are confronted with short life span of equipment and instruments that leads to high maintenance costs and low productivity. Friction causes the wear of machinery, accelerates decay of moving parts and decreases performance of instruments. Thus, decreasing the friction coefficient is necessary for low-cost, durable and energy-efficient machinery.

Physical vapour deposition magnetron sputtering technique [1], which does not affect the properties of the base material and biochemical functionality, is used for depositing tribological coatings for friction reduction and wear resistance. Such coatings have good adhesion and serve as a protective layer. Carbon-copper (a-C/Cu)

coatings are of particular interest [2]–[4]. Such coatings have a composite structure in which copper and graphite do not constitute carbide directly – copper nanoparticles are built in graphite matrix. a-C/Cu coatings are characterised with high mechanical and tribological quality index [5]; therefore, the present article researches these nanocoatings, aiming at obtaining the coefficient of surfaces with a low friction and, in compliance with it, the wear resistance.

2. EXPERIMENTAL PROCEDURE

30 mm dia. x 3mm chromium steel (100Cr6 after DIN 17230: 1980) plates were used as substrates. Prior to a deposition procedure, the ultrasonic cleaning of all samples using "Lotonaxe" degreasing bath was performed; then the water-alcohol mixture cleaning and drying with hot air were made.

Deposition equipment scheme is shown in Fig. 1**.** Base pressure of vacuum chamber is $1*10^{-3}$ Pa. Substrates were fixed on a two-fold rotating table and its surface was activated in argon atmosphere using ion-beam gun at 500 V bias potential and heated to a temperature of 350 ± 20 °C.

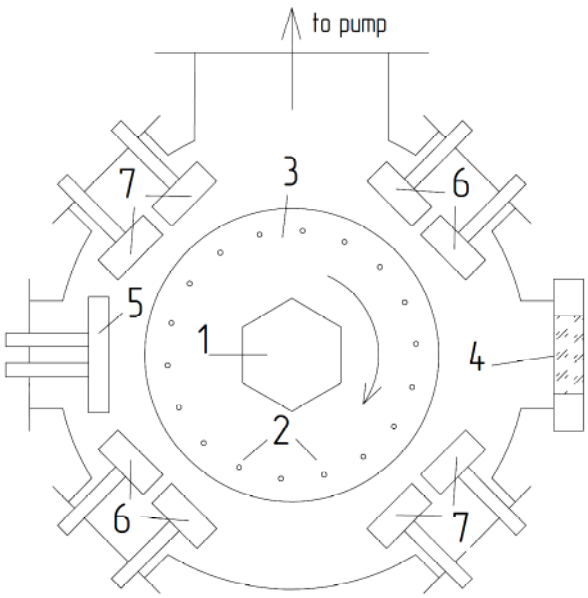

Fig. 1. Scheme of a vacuum sputtering system, 1 – heater, 2 – substrate holders, 3 – rotating table, 4 – view port, 5 – ion-beam gun, 6 – magnetrons with Ti targets, 7 – magnetrons with mosaic Cu-C targets (or Cu targets).

a-C/Cu nanocomposite films were deposited by high power DC magnetron sputtering process using high-performance industrial unit VU-SMA 600/4 [6]. Substrate-target distance of 100 mm and argon pressure pf 0.4 Pa were used during deposition. Cu/C mosaic type target with a 14–44 % carbon content supplied 7–40 at. % of carbon in the coatings. –100 V bias voltage was provided for a deposition

experiment. Power density on Cu/C 70 mm dia. targets (see Fig. 2) reached 50 W/cm^2, which ensured a deposition rate up to 0.10 μm/min. Power density on Ti targets varied in the interval of 10–50 W/cm^2 that resulted in titanium content of 5.5–19 at. %.

Fig. 2. Cu/C target.

In all the experiments, the coating was made of several layers: the first one was a 300 nm titanium layer, which provided coating adhesion, and the others were Cu-C and titanium nanolayers. Deposition experiment regimes are listed in Table 1.

Table 1

Cu/C Coating Deposition Regimes

No.	Coating type	Thickness, μm	P(Ti)/P(Total), %	P(Total), kW
1	CuC	5.3	0	9.2
2	CuC	8.5	0	9.2
3	CuC+Ti	10.3	14.8	10.8
4	CuC+Ti	8.6	30.3	13.2
5	CuC+Ti	8.5	41.0	15.6
6	CuC+Ti	6.8	49.5	18.2

After the deposition experiment, Ti percentage of the coating was determined. Atomic emission spectrometer Leco GDS850A was used for this purpose [7]. The samples were analysed with glow discharge excitation in direct current mode, with 4 mm anode at a constant voltage and current stabilisation (900 V, 30 mA). Ti percentage of the observed samples can be seen in Table 2.

Table 2

Ti Percentage of the Nanocoating

Sample No.	Ti, at.%
1, 2	0 %
3	5.5%
4	11%
5	15%
6	19%

3. EXPERIMENTAL PART

In order to evaluate the qualities of nanocoating surface use, it was important to look at coating surface microtopography and to specify 3D roughness parameters, as well as to conduct tribological experiments for determining friction coefficient and wear intensity.

Coating surface 3D microtopography measurements were made using *Taylor Hobson Form Talysurf Intra 50* profilometer. Measurement settings are shown in Table 3.

Table 3

3D Microtopography Measurement Settings

Stylus	Standard Stylus Arm 112/2009
Number of points (Y)	500
Data length (Y)	2 mm
Number of points (X)	500
Data length (X)	2 mm
Measurement speed	0.5mm/s

All microtopography images (Fig. 3) were processed in *Talymap Expert* software according to the following algorithm: 1) Form error was removed to obtain horizontal surface – primary surface; 2) Roughness was filtered from primary surface, using Gaussian filter and cut-off according to ISO 25178-2:2012 recommendations; 3) 3D roughness parameter Sa was calculated.

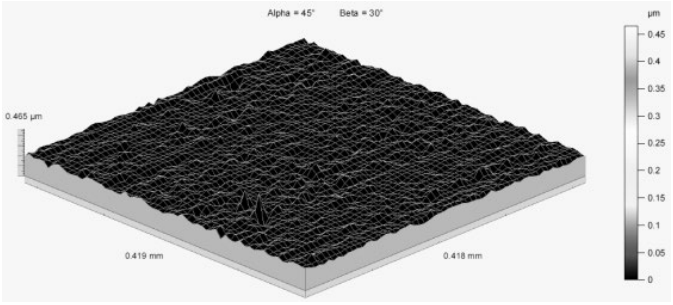

a

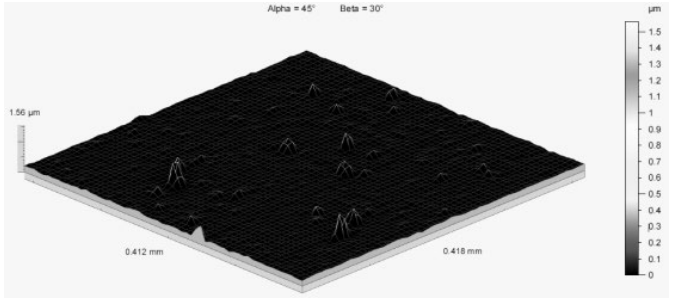

b

Fig. 3. Surface roughness of samples No.1 and No.5 after filtering.

Tribological experiments were performed on a *CSM Instruments* ball-on-disk type tribometer. Experiment settings are shown in Table 4.

Table 4

Tribological Experiment Settings

Ball material and size	100Cr6, Ø=6 mm
Applied load, F	2, 4, 6 N
Linear motion speed, v	0.05 m/s
Sample rotation cycles, n	1500 cycles
Tribotrack radius, R	3.0; 5.5 mm
Environment	Ambient air, dry friction

The experiments with 2N and 6N load were carried out with tribotrack radius (*R*) 3.0mm, but for 4N – with 5.5 mm radius, because of the limited sample surface area (see Fig. 4).

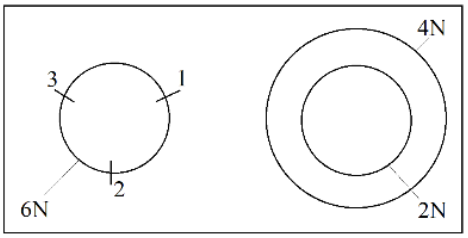

Fig. 4. Measurement location on the sample surface: 2N, 4N, 6N – tribotracks; 1, 2, 3 – cross-sectional area (A) measurement positions.

Friction coefficient (*COF*) was obtained as an average value from measurement, but tribotrack volume (W_v, mm^3) and wear rate (W_r, $mm^3/N{\cdot}m$) were calculated from tribotrack cross-sectional area (A, μm^2) measurement (see Fig. 5).

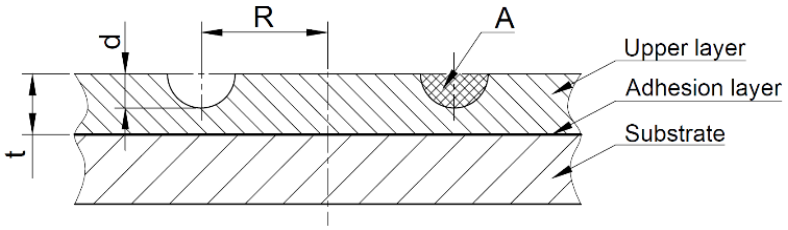

Fig. 5. Schematic image of sample cross-section after measurement
A – tribotrack cross-section area (μm²); R – tribotrack radius (mm); t – coating thickness (μm); d – tribotrack depth (μm).

Cross-sectional area was measured using *Taylor Hobson Surtronic 25* profilometer with *standard pick up 112/1502,* and values were calculated with *Talymap Gold 4.1* software built-in function *Surface of a Hole/Peak*. Final cross-sectional area result was calculated as an average from three independent measurements (angle between measurements ~ 120 º), see Fig. 4. Tribotrack wear volume in 1mm distance was calculated using the following equation:

$$W_v = A \cdot l_{1mm}, \quad (1)$$

where A – tribotrack cross-sectional area, mm^2;

l_{1mm} – 1 mm distance of tribotrack, mm.

The distance of 1mm for tribotrack wear volume calculations was chosen in order to compare material volume loss intensity for tribotracks with different radius *(R)*. Total tribotrack wear volume can be calculated by multiplying W_v by track circumference length.

Wear rate was calculated using the following equation [10]:

$$W_r = \frac{W_v}{F \cdot l}, \quad (2)$$

where W_v – tribotrack volume, mm^3;

F – load on ball, N;

l – total wear experiment distance, m.

4. RESULTS AND DISCUSSION

Surface 3D microtopography measurements were accomplished for all 6 samples in order to see how coating affects substrate roughness. From the acquired 3D roughness images and calculated parameters, the authors conclude that all coatings form isotropic surface texture, which is rougher than the one of substrate (arithmetic mean of the deviations from the mean plane for substrate – S_a*=9.04 nm*), on which coating is deposited (see Table 5). This fact can be explained by copper (Cu) tendency of forming peaky structure during the deposition process that increases the average value of surface roughness. It was also concluded that coatings with titanium (Ti) component show a tendency of having smoother surface than those without it. This can be explained by the fact that Ti particles replace Cu particles, thereby reducing Cu peak forming opportunity.

Tribological experiments with *F*=2 N, V=0.05 m/s, n=1500 cycles, R=3.0 mm were conducted. The obtained experiment data are summarised in Table 5.

Table 5

Experimental Measurement Data with 2N Applied Force

Sample	Ti, at., %	Sa, nm	t, µm	d, µm	A, µm^2	Wv, µm^3	Wr, mm^3/(N·m)	COF
1	0	9.64	5.30	0.8	52.8	5.28E-05	1.76E-05	0.189
2	0	13.60	8.50	0.91	40.20	4.02E-05	1.34E-05	0.187
3	5.5	10.50	10.30	0.43	15.77	1.58E-05	5.26E-06	0.229
4	11	9.90	8.60	0.79	48.43	4.84E-05	1.61E-05	0.256
5	15	9.12	8.50	0.23	8.97	8.97E-06	2.99E-06	0.189
6	19	10.20	6.80	0.31	17.57	1.76E-05	5.86E-06	0.226

Soft a-C/Cu coatings (samples No. 1 and 2) were analysed by comparing their parameters *t* and *d* (see Fig. 5), and it was found that coating of such soft a-C/Cu films was not valid for practical applications because of very low wear resistance, while reinforced coatings (samples No. 3 to 6) showed a noticeable increase in wear resistance, whereas *COF* increase was relatively small. In order to get more detailed information on the Ti influence on coating tribological parameters, the second part of experiment was performed for all reinforced coatings (samples No. 3 to 6) and also for the best one of soft a-C/Cu coatings (sample No. 2). In additional experiments, two differently applied loads (4N, 6N) were used in order to see how Ti concentration influences coating tribological parameters at different contact pressures. The obtained data are shown in Table 6.

Table 6

Experimental Measurement Data with 4N and 6N Applied Force

Sample	Ti, at. %	COF		d, μm		Wv, μm^3		Wr, mm^3/(N·m)	
		4N	6N	4N	6N	4N	6N	4N	6N
2	0	0.179	0.167	0.74	2.23	3.53E-05	1.23E-04	5.88E-06	1.37E-05
3	5.5	0.243	0.258	1.54	2.14	1.02E-04	1.79E-04	1.70E-05	1.90E-05
4	11	0.267	0.267	1.14	1.24	6.85E-05	1.05E-04	1.14E-05	1.16E-05
5	15	0.207	0.225	0.96	1.67	2.56E-05	5.11E-05	4.27E-06	5.68E-06
6	19	0.242	0.210	0.50	0.72	3.90E-05	4.37E-05	6.50E-06	4.86E-06

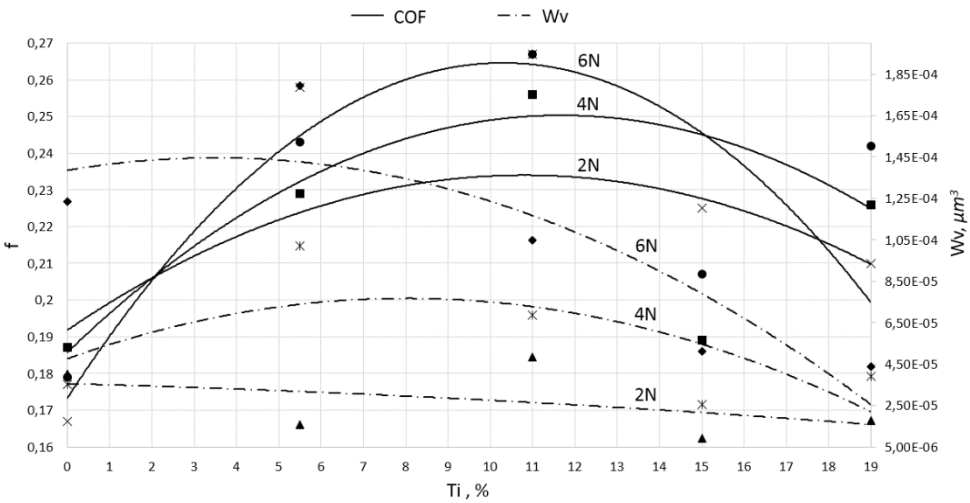

Fig. 6. Ti concentration influence on tribotrack wear volume (Wv) and coefficient of friction (COF).

Figure 6 shows that *COF* values tend to increase until Ti concentration reaches ~11 at. %, and then decreases. It can be seen that *COF* overall values tend to be bigger if the applied load is increased; it can be explained by the fact that a bigger applied load tends to penetrate tribometer ball deeper into the coating, thus resulting in greater surface microcutting. Coating wear volume curves tend to copy *COF* curves, but after Ti concentration reaches ~11 at. %, wear resistance increases rapidly, especially if a greater applied load is used, thus proving that coating reinforcing

with Ti can significantly improve their overall tribological parameters. Experimental data show that the best tribological parameters are shown by sample No. 5 that has Ti concentration of 15 %.

5. CONCLUSIONS

In the present research, it has been stated that at the a-C/Cu coating deposition the surface properties are different, which is linked to the composition of nanocoating. When depositing Ti adhesive layer and then Cu-C layer at different deposition modes, the values of coating wear resistance and the coefficient of friction change. After adding titanium to the a-C/Cu layer and varying its percentage composition, it can be concluded that the coefficient of friction increases at Ti concentration raising to 11 %, but wear volume values do not alter significantly. The coefficient of friction and wear volume decrease after further rise in Ti concentration. Consequently, it can be seen that the optimal coating wear resistance is at 11 % Ti concentration.

ACKNOWLEDGEMENTS

The research has been supported by the European Regional Development Fund within the project No. 2014/0011/2DP/2.1.1.1.0/13/APIA/VIAA/005.

REFERENCES

1. Safi, I. (2000). Recent aspects concerning DC reactive magnetron sputtering of thin films. *Surface & Coatings Technology,* 127 (2–3), 203–219.
2. Berman, D., Erdemir, A., and Sumant, V. A. (2013). Few layer graphene to reduce wear and friction on sliding steel surfaces. *Elsevier, Carbon 54*, 454–459.
3. Chan, Y. H., Huang, C. F., Ou, K. L., and Peng, P. W. (2011). Mechanical properties and antibacterial activity of copper doped diamond-like carbon films. *Surface & Coatings Technology.* 206 (6), 1037–1040.
4. Cabioc'h, T., Naudon, A., Jaouen, M., Thiaudiére, D., and Babonneau, D. (1999). Co-sputtering C-Cu thin film synthesis: Microstructural study of copper precipitates encapsulated into a carbon matrix. *Philosophical Magazine Part B,* 79 (3), 501–516.
5. Musil, J., Louda, M., Soukup, Z., and Kubásek, M. (2008). Relationship between mechanical properties and coefficient of friction of sputtered a-C/Cu composite thin films. *Diamond & Related Materials*, 17 (11), 1905–1911.
6. Mitin, V., Sharipov, E., and Mitin, A. (2006). High deposition rate magnetrons – innovative coating technology: Key elements and advantages. *Surface Engineering,* 22 (1), 1–6.
7. Fernández, B., Pereiro, R., Sanz-Medel, A. (2010). Glow discharge analysis of nanostructured materials and nanolayers. *Analytica Chimica Acta,* 679 (1–2), 7–16.

AR TITĀNU PASTIPRINĀTU PVD VARA-OGLEKĻA KOMPOZĪTU PĀRKLĀJUMU TRIBOLOĢISKĀS ĪPAŠĪBAS

J. Lungevics, A. Leitāns, J. Rudzītis,
N. Bulahs, P. Nazarovs, V. Kovaļenko

K o p s a v i l k u m s

Dotajā rakstā apskatīta dažādu pārklājumu ietekme, kas palielina virsmu nodilumizturību. Rakstā tika analizēti seši a-C/Cu nanopārklājumi, kuri atšķiras ar Ti koncentrāciju. Pētāmie paraugi tika pakļauti metroloģiskām un triboloģiskām pārbaudēm; Tika nomērīti virsmas raupjuma parametri ar mēriekārtu *Taylor Hobson Talysurf Intra 50* un berzes koeficients ar *CSM Instruments ball-on-disk type tribometer*, un papildus aprēķināti dilšanas intensitāte un dilušās zonas šķērsgriezuma laukums. Pārbaudes eksperimentu laikā tika noteikts raupjuma parametrs Sa un berzes koeficients pie trim dažādām slodzēm: 2N, 4N, 6N. Iegūts, ka pie lielākas Ti koncentrācijas berzes koeficients samazinās, it īpaši tas ir izteicams pie lielākām slodzēm, savukārt dilšanas intensitātes vērtībām ir tendence no sākuma palielināties, pieaugot Ti koncentrācijai līdz aptuveni 11%, bet pēc tām samazināties, nodrošinot tādā veidā labāku nanopārklājuma dilumizturību.

13.07.2015.

MISTAKE CORRECTION

In the paper: S. Gendelis, A. Timuhins, A. Laizans, L. Bandeniece (2015). Latv. J. Phys. Tec. Sci., 52 (6), 49–60,

Acknowledgement* The name of the Fund is incorrect.

**ACKNOWLEDGEMENT*

The current research has been supported by the European Regional Development Fund (ERAF) (project No. L-KC-11-0005).

INFORMATION ON SUBSCRIPTION OF THE JOURNAL FOR YEAR 2016

Index: 2091 (to individual subscribers),
2092 (to collective subscribers)
Periodicity: bi-monthly

Price:

	individual subscribers	collective subscribers
per 2 months	EUR 1.50	EUR 15.00
per 4 months	EUR 3.00	EUR 30.00
per 6 months	EUR 4.50	EUR 45.00
per 8 months	EUR 6.00	EUR 60.00
per 10 months	EUR 7.50	EUR 75.00
per 12 months	EUR 9.00	EUR 90.00

Institute of Physical Energetics
Latvian reg. No. LV90002128912, Aizkraukles ielā 21,
Rīga, LV-1006, LATVIA
SEB banka
Account No LV 59UNLA 0001 5450 7025 7
Code: UNLALV2X

Contact person:

S. Ezerniece
tel. 67551732,67558694
http://fei-web.lv
ezerniec@edi.lv

LATVIAN JOURNAL of PHYSICS and TECHNICAL SCIENCES